https://doi.org/10.5194/egusphere-2026-1091
Preprint. Discussion started: 6 March 2026

Cloud vertical structure across China from a national Ka-band cloud radar network: Thermodynamic, dynamical, and land-surface controls

Hui Xu[1], Jianping Guo[1,2*], Jianbo Deng[3], Rongfang Yang[4,5], Deli Meng[6], Zhen Zhang[1], Ning Li[1], Yuping Sun[1], Shuairu Jiang[1], Tianmeng Chen[1], Juan Chen[7], Liping Zeng[8], Yongshui Zhou[9], Bing Tong[10]

[1]*State Key Laboratory of Severe Weather Meteorological Science and Technology, Chinese Academy of Meteorological Sciences, Beijing, 100081, China*

[2]*CMA Field Scientific Experiment Base for Low-Altitude Economy Meteorological Support of Unmanned Aviation in Guangdong-Hong Kong-Macao Greater Bay Area, Shenzhen 518108, China*

[3]*Hunan Meteorological Research Institute, Changsha, 410118, China*

[4]*China Meteorological Administration Xiong'an Atmospheric Boundary Layer Key Laboratory, Xiong'an New Area, 071800, China*

[5]*Hebei Meteorological Technology and Equipment Center, Shijiazhuang 050022, China*

[6]*National Institute of Natural Hazards, Ministry of Emergency Management of China, Beijing 100085, China*

[7]*AVIC Leihua Electronic Technology Research Institute, Wuxi 214063, China*

[8]*Guizhou New Meteorological Technology Co., Ltd, Guiyang 550001, China*

[9]*Meteorological Observatory of Guizhou, Guiyang 550001, China*

[10]*State Key Laboratory of Regional and Urban Ecology, Research Center for Eco-environmental Sciences, Chinese Academy of Sciences, Beijing, 100085, China*

Correspondence to: Dr./Prof. Jianping Guo (Email: jpguocams@gmail.com)

https://doi.org/10.5194/egusphere-2026-1091
Preprint. Discussion started: 6 March 2026

Abstract

Cloud vertical structure plays a central role in regulating Earth's radiation balance and hydrological cycle, yet it remains poorly represented in weather and climate models due to limited high-resolution observations. Using a newly established national network of 80 Ka-band cloud radars, we provide the first high-spatiotemporal-resolution characterization of cloud vertical structure across China for 2024 and quantify its thermodynamic, dynamical, and land-surface controls. An improved retrieval algorithm accounting for height-dependent radar sensitivity and clutter suppression is applied to derive cloud boundaries. The national annual mean cloud occurrence frequency is 56.7%, dominated by single-layer clouds (34.7%), followed by two-layer (14.7%) and multi-layer clouds (7.1%). Single-layer clouds prevail over arid northwestern China, whereas multi-layer clouds are more frequent in humid southeastern regions. Cloud base height exhibits strong seasonality, with higher values in summer and lower values in winter, and distinctly lower bases over the Tibetan Plateau. Diurnally, summer clouds show a pronounced afternoon peak between 3 and 9 km, while winter clouds are mainly confined below 3 km with a near-sunrise maximum. Thermodynamic conditions exert primary control on cloud vertical development. Higher low-level humidity favors deeper clouds and higher tops, whereas stronger lower-tropospheric stability suppresses vertical growth. Wind shear generally limits cloud depth, though moderate shear may enhance organization under unstable conditions. Land-surface characteristics further modulate cloud base height, with higher bases over barren land and lower bases over forests. These results provide national-scale observational benchmarks for improving cloud parameterizations in numerical models.

Short Summary

Using a new national network of 80 cloud radars, we mapped how clouds are layered and how high they reach across China. Clouds vary strongly by region, season, and time of day, with deeper clouds in humid, unstable conditions and shallower clouds in stable or windy conditions. Also, land cover matters: forests tend to have lower cloud bases than barren land. These findings help improve weather and climate predictions.

https://doi.org/10.5194/egusphere-2026-1091
Preprint. Discussion started: 6 March 2026

1. Introduction

Clouds are a crucial component of the Earth-atmosphere system and exert strong influence on both global and regional climate, as well as the hydrological cycle (Ramanathan et al., 1989; Stephens et al., 2005; Williams et al., 2006; Bony et al., 2015; Voigt et al., 2021). By reflecting and scattering incoming solar shortwave radiation and absorbing outgoing longwave radiation, clouds substantially modulate the radiation budget at the top of the atmosphere, within the atmosphere, and at the surface (Wielicki et al., 1995; Muhlbauer et al., 2014; Xu et al., 2021; Li et al., 2023). Cloud macrophysical characteristics—including cloud fraction, cloud base height (CBH), cloud top height (CTH), cloud thickness (CT), and the number of vertical layers—strongly influence cloud radiative forcing and precipitation processes (Weare, 2000; Wild, 2012; George et al., 2018; Zhang et al., 2019). Despite decades of research, climate models continue to exhibit substantial biases in simulating these cloud macrophysical properties, contributing significantly to considerable uncertainties in climate projections (Cesana and Waliser, 2016; IPCC, 2021; Cesana et al., 2022). For instance, many global climate models tend to overestimate high-level clouds in moist environments while underestimating low-level clouds in dry environments (Cesana and Waliser, 2016). Improving the representation of cloud vertical structure (CVS) is therefore essential for reducing model uncertainty and enhancing the reliability of weather and climate simulations.

Satellite observations provide broad spatial coverage of cloud macrophysical properties. Passive sensors such as the Moderate Resolution Imaging Spectroradiometer (MODIS) and the Multiangle Imaging Spectroradiometer (MISR) have been widely used to retrieve CTH and related properties. Based on two decades (2002–2021) of MODIS data, Richardson et al. (2022) reported an increasing trend in tropical-mean high-cloud altitude of 6.9 ± 2.7 m yr^{-1}, which is statistically consistent with climate model projections. Using MISR-derived CTHs, Chae and Sherwood (2010) investigated the relationship between environmental stability and tropical deep convective cloud altitude over the western Pacific, finding altitude variations of approximately 2 km associated with higher convective available potential energy (CAPE). More recently, Mitra et al. (2023) combined MODIS and MISR data to improve CTH retrieval for thin cirrus overlying low-level clouds. However, passive sensors generally lack the capability to resolve cloud vertical structure comprehensively, particularly CBH and multi-layer configurations.

Active satellite instruments, including the Cloud Profiling Radar (CPR) aboard CloudSat and the Cloud-Aerosol Lidar with Orthogonal Polarization (CALIOP) aboard CALIPSO, have greatly advanced CVS observations (Stephens et al., 2002; Mace et al., 2007; Marchand et al., 2008; Huang et al., 2015). Using combined CloudSat and CALIPSO data, Oreopoulos et al. (2017) identified single-layer low and high clouds as the most frequent global CVS types, accounting for approximately 53% of cloudy scenes. Over China, Chi et al. (2022) documented strong regional and seasonal variability in CBH and CTH.

https://doi.org/10.5194/egusphere-2026-1091
Preprint. Discussion started: 6 March 2026

Nevertheless, active satellite retrievals have limitations. Compared with surface-based observations, CloudSat–CALIPSO products underestimate low clouds, missing approximately 25% of clouds below 600 m and 9% between 600 m and 1 km (Liu, 2022). Moreover, their narrow swath width and 16-day revisit cycle restrict temporal sampling and limit the ability to resolve diurnal variability.

Radiosonde observations provide high-vertical-resolution temperature and humidity profiles, allowing for the retrieval of CVS. Threshold-based methods have been widely used for CVS retrieval, including the dew-point depression technique (Poore et al., 1995), fixed relative humidity thresholds (Wang and Rossow, 1995), second-derivative methods (Chernykh and Eskridge, 1996), and dynamic altitude-dependent RH thresholds (Zhang et al., 2010). Xu et al. (2023) developed an improved retrieval method incorporating humidity and temperature gradients, revealing regional differences in low-cloud occurrence across East Asia, Europe and North America. However, these sounding measurements are typically conducted twice daily at 0000 UTC and 1200 UTC (Guo et al., 2016, 2019; Zhou et al., 2020), making them insufficient to capture the full diurnal evolution of CVS.

Compared with radiosonde observations, ground-based Ka-band millimeter-wave cloud radar (MMCR) enables continuous monitoring of CVS (Shupe et al., 2008). Owing to its high spatiotemporal resolution and strong penetration capability (Moran et al., 1998; Hollars et al., 2004), MMCR has been widely applied to analyze diurnal and seasonal variations in CVS (Zhao et al., 2017; Zhou et al., 2019; Chen et al., 2022). However, most MMCR based studies on CVS have been limited to individual sites or small regions, leaving a systematic national-scale characterization of CVS largely unexplored. Previous research has highlighted that cloud vertical development is jointly influenced by atmospheric thermal conditions, dynamical processes, and land-surface characteristics (Richardson, 2007; Chen et al., 2015; Fu et al., 2020). Specifically, lower-tropospheric stability (LTS) and low-level humidity are key thermodynamic factors regulating boundary-layer development and CBH, while vertical wind shear modulates CTH and CT by influencing the vertical development of clouds (Helfer et al., 2020; Wang et al., 2020; Yang et al., 2022; Xu et al., 2025). Land cover types further modulate cloud formation and CVS by altering surface energy partitioning and moisture fluxes (Wang et al., 2021). Despite these advances, most studies have focused on isolated factors or localized regions. To our knowledge, no previous study has ever provided a national-scale, high-frequency characterization of CVS across China using a coordinated ground-based radar network, nor systematically quantified the combined thermodynamic, dynamical, and land-surface controls.

To address this gap, we present the first attempt to retrieve high-spatiotemporal-resolution vertical structures of clouds across China using one year (2024) of MMCR observations from a national network of 80 stations. The retrieved CVS metrics include cloud layer number, CBH, CTH, and CT for each

https://doi.org/10.5194/egusphere-2026-1091
Preprint. Discussion started: 6 March 2026

detected cloud layer. An improved retrieval algorithm incorporating height-dependent radar sensitivity curves and a variance-based clutter suppression method is developed to enhance detection reliability. Unless otherwise specified, CBH refers to the base height of the lowest cloud layer, CTH denotes the top of the highest cloud layer, and CT represents the total cloud thickness, defined as the difference between CTH and CBH.

The remainder of this paper is organized as follows: Section 2 describes the observational data and methodology used for CVS retrieval. Section 3 presents the spatial, vertical, seasonal, and diurnal characteristics of CVS and analyzes its thermodynamic, dynamical, and land-surface controls. Section 4 summarizes the main findings and discusses their implications for weather and climate modeling.

2. Data and methods

2.1 Study area

China spans a vast territory across broad latitudinal and longitudinal ranges, leading to pronounced spatial heterogeneity in both atmospheric and surface conditions. The climate is predominantly governed by the Asian monsoon systems and the topographic forcing of the Tibetan Plateau, which together result in substantial regional variations (Ye and Gao, 1979; Domroes and Peng, 1988; Ding and Murakami, 1994). In eastern China, a distinct north–south gradient is evident: southern regions are characterized by year-round warm and humid conditions, while northern areas experience colder winters and pronounced seasonal temperature variability. In contrast, western China, an area dominated by high-elevation terrain such as the Tibetan Plateau, is typified by low temperatures, strong radiative cooling, and limited moisture availability (Shi and Wang, 2020). Across this diverse landscape, meteorological variables exhibit strong seasonal cycles: precipitation and air temperature peak in summer (June–July–August) and reach minima in winter (December–January–February), sunshine duration follows a similar seasonal pattern, with maximum values occurring in summer. Wind speeds are generally highest in spring (March–April–May), whereas relative humidity remains consistently elevated in southern China and shows comparatively modest seasonal variation. Autumn (September–October–November) does not display equally distinct seasonal extremes in these meteorological variables.

2.2 Data

2.1.1 Ka-band millimeter-wave cloud radar observations

The MMCRs retrieve cloud macrophysical properties by detecting the scattering signals of cloud particles at millimeter wavelengths (Hobbs et al., 1985; Kollias et al., 2007). Capable of continuously

https://doi.org/10.5194/egusphere-2026-1091
Preprint. Discussion started: 6 March 2026

monitoring cloud vertical structure with high spatiotemporal resolution (Clothiaux et al., 2000; Mace et al., 2001; Hollars et al., 2004), the MMCRs employed in this study operates with a vertical resolution of 30 m, a temporal resolution of 1 minute, and a maximum detection height of 18 km above ground level (AGL). Compared to conventional weather radars, the shorter wavelength of the MMCRs enhances their sensitivity to small cloud particles, making them particularly effective for observing non-precipitating and weakly precipitating clouds, as well as for penetrating multi-layer cloud systems (Moran et al., 1998; Kollias et al., 2007). This penetrative ability enables MMCRs to obtain detailed vertical cloud profiles, especially for thick, dense, and multi-layered clouds.

MMCR data have been widely used in cloud boundary detection (e.g., Zhang et al., 2017; Zhou et al., 2019; Fang et al., 2023) and exhibit strong consistency with radiosonde observations (Wang et al., 2016; Zhao et al., 2017; Chen et al., 2022). In this study, MMCR data for the year of 2024 were obtained from the China Meteorological Administration (CMA). Of the 120 MMCR stations operating across China in 2024, only those with at least 100 valid observation days annually were retained to ensure data quality. This criterion resulted in the selection of 80 stations for subsequent analysis (Fig. 1).

2.2.3 Radar wind profiler measurements

The radar wind profiler (RWP) is a ground-based remote sensing instrument designed to measure wind vertical profiles within the planetary boundary layer (PBL) and the lower free atmosphere (Liu et al., 2020). By transmitting electromagnetic beams in multiple directions and analyzing the returned signals, the RWP provides a comprehensive set of atmospheric variables, including horizontal wind speed and direction, vertical velocity, radial velocity, Doppler spectral width, signal-to-noise ratio (SNR), and the refractive index structure parameter (C_n^2) (Liu et al., 2020). These measurements typically cover altitudes from 150 m to 5.0 km AGL, with a vertical resolution of 120 m and a temporal interval of 6 minutes (McCaffrey et al., 2017; Ruan et al., 2014). Compared to conventional radiosonde observations and reanalysis datasets, RWPs offer significantly higher temporal resolution, thereby facilitating high-resolution, continuous monitoring of temporal variations in atmospheric wind profiles. In this study, vertical wind shear at 700 hPa (WS_{700}) was derived from RWP observed wind speed and direction profiles using the following formula:

$$S = \left[\left(\frac{\partial u}{\partial h}\right)^2 + \left(\frac{\partial v}{\partial h}\right)^2\right]^{1/2} \quad (1)$$

where S denotes the vertical wind shear, and u and v represent the zonal and meridional components of the horizontal wind, respectively.

https://doi.org/10.5194/egusphere-2026-1091
Preprint. Discussion started: 6 March 2026

Despite these advantages, RWP measurements are subject to notable uncertainties. Data quality is often degraded below approximately 0.5 km AGL due to near-surface clutter, while significant beam attenuation limits reliable detection above about 5.0 km AGL. Therefore, rigorous quality control is essential before deriving dynamic variables from RWP data. In practice, only observations within the 0.5–5.0 km height range are generally considered suitable for reliable analysis, which ensures the accuracy of WS_{700} calculations (consistent with the height range of the lower free atmosphere targeted by RWP measurements).

2.2.3 ERA5 reanalysis

ERA5, the latest global atmospheric reanalysis produced by the European Centre for Medium-Range Weather Forecasts (ECMWF), was released in 2017 and provides continuous meteorological data from January 1950 to the present (Bell et al., 2021). Generated using a 4-dimensional variational (4D-Var) data assimilation system, ERA5 offers comprehensive, high-resolution, and large-scale meteorological fields that are well suited for climatic research, with temporal and spatial resolutions of up to 1 hour and 0.25°×0.25° (approximately 31 km), respectively (Hersbach et al., 2020). ERA5's fine resolution facilitates improved representation of vertical profiles and diurnal variations in key atmospheric variables, particularly over land areas (Dai, 2023). In this study, we use ERA5 data for 2024 to examine the impacts of LTS and specific humidity on CVS. For this purpose, hourly temperature at 1000 hPa and 700 hPa, and specific humidity at 850 hPa (q_{850}) are extracted for all 80 selected MMCR stations.

To quantify the thermal stratification of the lower troposphere, LTS was derived following the formulation proposed by Wood and Bretherton (2006), which is defined as the difference in potential temperature between the 700 hPa and 1000 hPa pressure levels:

$$LTS = \theta_{700\,hPa} - \theta_{1000\,hPa} \quad (2)$$

where θ denotes the potential temperature, calculated using the following formula:

$$\theta = \mathrm{T}\left(\frac{p_0}{p}\right)^{\frac{R}{C_p}} \quad (3)$$

where T and p represent the air temperature and atmospheric pressure at the given pressure level, respectively; p_0 = 1000 hPa is the reference pressure; R is the specific gas constant for dry air; and C_p is the specific heat capacity at constant pressure.

2.3 CVS retrieval methods based on MMCR data

MMCR identifies cloud boundaries by detecting radar backscatter from hydrometeors, including liquid droplets and ice crystals within clouds. However, due to its short operating wavelength, MMCR is

https://doi.org/10.5194/egusphere-2026-1091
Preprint. Discussion started: 6 March 2026

also sensitive to non-meteorological echoes, such as near-surface dust, insect swarms, and atmospheric turbulence, as well as random noise arising from instrumental instabilities and signal processing artifacts (Ulaby et al., 1981; Zhou, 2008). These interfering signals can degrade the reliability of cloud boundary detection and introduce biases in retrieved CVS.

A commonly used approach for retrieving CVS is the reflectivity threshold approach, which distinguishes cloud signals from background noise and clutter using a fixed reflectivity cutoff. Based on MMCR observations from the U.S. Atmospheric Radiation Measurement (ARM) program, Clothiaux et al. (1999) reported that radar reflectivity (Z) for various cloud types—including cirrus, stratus, and precipitating clouds—typically ranges from –50 dBZ to 20 dBZ. Consequently, many previous studies have adopted a constant minimum threshold of approximately –40 dBZ for cloud detection (e.g., Zhang et al., 2019; Chen et al., 2022; Fang et al., 2023).

However, the fixed threshold neglects the height-dependent sensitivity of radar measurements. Because radar detectability decreases with range, weak high-altitude cloud signals may fall below a constant threshold, while near-surface clutter may be misclassified as clouds. Such biases can lead to inaccurate estimates of cloud occurrence and vertical structure.

To address these limitations, this study introduces an improved CVS retrieval technique that integrates (1) theoretical radar sensitivity curves accounting for height-dependent detection capability and (2) a variance-based clutter suppression method adapted from Kalapureddy et al. (2018). By combining physically constrained sensitivity thresholds with statistical filtering of reflectivity variability, this approach enhances cloud detection robustness across different altitudes and cloud regimes.

The retrieval procedure consists of the following steps:

First, a height-dependent noise-equivalent reflectivity (NER) threshold curve (denoted as $Z_{th}(j)$) is established to replace the fixed threshold. This curve is tailored to typical atmospheric conditions over China and defined as:

$$Z_{th}(j) = \sqrt{1.2 \times j} - 42.0 \quad (4)$$

where j represents the vertical range bin index (or corresponding height level). This formulation accounts for the progressive reduction in radar sensitivity with increasing height.

For a given time t, the measured reflectivity $Z(j,t)$ at height level j is classified as a potential cloud signal if:

$$Z(j,t) \geq Z_{th}(j) \quad (5)$$

Otherwise, the signal is classified as noise. This step generates a preliminary binary indicator $I(j,t)$, where $I = 1$ denotes potential cloud signals and $I = 0$ denotes noise. The resulting non-noise layers provide the initial candidates for cloud detection while removing the majority of random noise.

https://doi.org/10.5194/egusphere-2026-1091
Preprint. Discussion started: 6 March 2026

To further refine the non-noise regions, contiguous segments where $I(j,t) = 1$ are identified as candidate cloud-containing layers. Although the NER threshold removes most random noise, residual non-meteorological clutter may remain. To further distinguish true cloud signals from clutter, a variance-based method is applied within the identified non-noise layers. This method exploits the physical property that cloud hydrometeors are generally more spatially homogeneous and temporally coherent than clutter sources (Kalapureddy et al., 2018). As a result, the temporal variability of reflectivity within cloud-dominated layers is typically lower than that within clutter-contaminated layers.

A 3-minute sliding time window is applied at each height level within the non-noise layers. Within each window, the standard deviation of reflectivity across consecutive profiles is calculated, forming a variability sequence Ai. The mean (μ) and standard deviation (σ) of this sequence are then calculated as:

$$\mu = \frac{1}{3}\sum_{i=0}^{2} A_i \quad (6)$$

$$\sigma = \left[\frac{1}{3}\left(\sum_{i=0}^{2}(A_i - \mu)^2\right)\right]^{\frac{1}{2}} \quad (7)$$

A dual-threshold criterion is applied to identify moist (cloud) layers: if $\mu < 2.0$ dBZ, and $\sigma < 1.0$ dBZ. If both conditions are satisfied, the signal at that height is identified as part of a moist layer. The base and top height levels of moist (cloud) layers are determined by identifying vertically contiguous bins meeting this criterion. Otherwise, the segment is filtered out as clutter.

Finally, the cloud detection step is conducted to retrieve the CBH and CTH of each identified cloud layer by verifying the radar reflectivity within previously detected moist layers. This step yields the final CVS. Specifically, any candidate moist layer with a maximum reflectivity lower than −20 dBZ is excluded, as such weak backscatter signals are unlikely to represent physically meaningful cloud layers and may instead reflect residual noise or sub-detection-limit echoes. This reflectivity threshold is selected to balance sensitivity to thin non-precipitating clouds and robustness against noise contamination.

Given the high temporal resolution (1 min) of the MMCR observations, loosely connected cloud elements may occasionally be misidentified as multiple discrete layers. To reduce artificial layer fragmentation, an additional quality-control procedure is applied to the initially detected cloud boundaries. For each identified cloud layer, both its geometric thickness and the vertical separation distance to adjacent layers are calculated. If a cloud layer is thinner than 7 range bins (equivalent to 210 m at the 30 m vertical resolution of the MMCR), the following criteria are applied:

- If the separation distance to the nearest adjacent cloud layer exceeds 24 range bins (720 m), the thin layer is considered isolated and is discarded.
- If the separation distance is less than or equal to 24 range bins, the thin layer is merged with the nearest adjacent cloud layer.

https://doi.org/10.5194/egusphere-2026-1091
Preprint. Discussion started: 6 March 2026

This procedure reduces spurious detections while preserving physically coherent multi-layer structures. The complete CVS retrieval workflow is illustrated in the flowchart (Fig. 2). The algorithm is capable of detecting cloud layers across a wide range of altitudes and configurations, including single-layer, multi-layer, shallow, and deep convective structures. An example case demonstrating the robustness of the retrieval under complex vertical conditions is provided in Fig. S1.

3. Results and discussion

This section presents the spatial, vertical, seasonal, and diurnal characteristics of cloud vertical structure across China, followed by an analysis of the thermodynamic, dynamical, and land-surface controls governing cloud development. Unless otherwise specified, statistics are derived from all valid MMCR observations in 2024 across the 80 selected stations.

3.1 Spatial distribution of cloud layer occurrence frequency

Figure 3 illustrates the spatial distributions of annual mean occurrence frequencies for total clouds and for clouds classified by vertical layer number (single-layer, two-layer, and multi-layer; the latter defined as three to five layers) across China under all-sky conditions in 2024. The national mean total cloud occurrence frequency is 56.7%, with regional values ranging from 40% to 70% (Fig. 3a). This value is slightly lower than the long-term mean cloud fraction of approximately 61% derived from MODIS observations during 2003–2018 (Zhao et al., 2019), potentially reflecting the reported declining trend in total cloud fraction over East Asia in recent years (Zhou et al., 2022). The probability density function (PDF) of total cloud occurrence frequency exhibits a non-uniform distribution, with high probabilities concentrated toward the upper end of the frequency range.

When classified by vertical structures (Figs. 3b–d), occurrence frequencies range from 25% to 40% for single-layer clouds, 10% to 16% for two-layer clouds, and 1% to 12% for multi-layer clouds. The PDF for single-layer clouds shows a relatively continuous distribution, with a concentration of stations at higher occurrence frequencies. In contrast, the PDF for two-layer clouds exhibits a more discontinuous pattern, with probability mass clustered in the high-frequency interval. Nationally averaged occurrence frequencies decrease systematically with increasing layer number, with mean values of 34.8% ± 4.0% for single-layer clouds, 14.7% ± 3.2% for two-layer clouds, and 7.1% ± 2.4% for multi-layer clouds.

These results indicate that single-layer clouds constitute the dominant vertical structure over China. This overall distribution is broadly consistent with CALIPSO-based estimates reported by Pan et al. (2016), although differences in magnitude likely reflect differences in observational platforms and sampling characteristics.

https://doi.org/10.5194/egusphere-2026-1091
Preprint. Discussion started: 6 March 2026

Spatially, the highest total occurrence frequencies are observed over the southeastern Tibetan Plateau and the Sichuan Basin (Fig. 3a). This pattern agrees with previous satellite-based studies (e.g., Pan et al., 2015; Yin et al., 2015) and can be attributed to topographic lifting and enhanced moisture convergence associated with complex terrain. However, the spatial contrast between northwestern and southeastern China differs somewhat from satellite-derived cloud fraction patterns. In particular, point-based MMCR observations indicate relatively higher total cloud occurrence frequencies at some stations in northwestern China compared with southeastern regions (Fig. 3b). This apparent discrepancy likely arises from fundamental differences in observational sampling: satellite products represent areal cloud fraction over large grid cells, whereas MMCR measurements capture local, vertically resolved cloud occurrence. In addition, northwestern China is often characterized by persistent, optically thin cloud layers, while southeastern China experiences more intermittent but vertically extensive convective systems. These differing cloud regimes may contribute to the observed spatial contrasts.

Single-layer clouds occur more frequently in northwestern China than in the southeast (Fig. 3b), whereas multi-layer clouds exhibit the opposite pattern, with higher frequencies in the southeast and lower frequencies in the northwest (Fig. 3d). This regional contrast likely reflects differences in moisture availability and atmospheric instability. Southeastern China, influenced by abundant water vapor transport and stronger solar heating, favours deep convective development and the formation of vertically complex, multi-layered cloud systems (Chi et al., 2022). In contrast, the comparatively dry and stable conditions in northwestern China promote simpler, predominantly single-layer cloud structures (Chen et al., 2019). No pronounced spatial gradient is evident for two-layer cloud occurrence under all-sky conditions (Fig. 3c), suggesting a more transitional vertical structure between the two dominant regimes.

3.2 Horizontal distribution of cloud height

CBH, CTH, and CT are fundamental descriptors of cloud vertical structure. CBH plays a particularly important role in regulating near-surface radiation and turbulent energy exchange, while also linking surface-atmosphere interactions to cloud formation processes. Accurate characterization of CBH is therefore essential for both regional weather forecasting and climate change assessments (e.g., Stephens et al., 2012; Mülmenstädt et al., 2018; An et al., 2019).

Figure 4 presents the horizontal distribution of seasonal mean CBH across China in 2024. CBH exhibits pronounced seasonal variability. In summer, CBH is generally elevated, with 84% of stations exceeding 3 km and approximately 10% reaching values up to 5 km (Fig. 4b). Spring (Fig. 4a) displays a similar spatial distribution but with lower magnitudes, with most CBH values (67%) concentrated between 2.5 km and 4 km. In contrast, autumn and winter (Figs. 4c-d) are characterized by substantially

https://doi.org/10.5194/egusphere-2026-1091
Preprint. Discussion started: 6 March 2026

lower CBH, predominantly within the 2–3 km range, and only a small fraction of stations exceeding 4 km. The seasonal mean CBH follows the order: summer (3.95 ± 0.88 km) > spring (3.24 ± 0.77 km) > autumn (2.78 ± 0.62 km) > winter (2.15 ± 0.89 km). This seasonal progression is consistent with previous studies (e.g., Shupe et al., 2011; Chi et al., 2022; Xu et al., 2023) and reflects the strong modulation of cloud formation by radiative forcing and boundary-layer dynamics. Enhanced solar heating in summer deepens the PBL and promotes stronger turbulent mixing, favouring higher cloud bases. In contrast, reduced insolation and increased static stability in winter suppress boundary-layer growth, resulting in lower CBH (Zhang et al., 2018).

Spatially, elevated summer CBHs (>3 km) dominate much of eastern China. While the East Asian summer monsoon enhances moisture transport from the Pacific (Ding and Chan, 2005; Li et al., 2016), increased surface heating and boundary-layer development over land can elevate condensation levels despite enhanced humidity. This highlights the competing influences of moisture supply and boundary-layer dynamics on CBH.

Over the Tibetan Plateau, CBH is distinctly lower (approximately 2.5 km above ground level) during spring and summer compared with surrounding regions. This regional feature reflects unique thermodynamic conditions associated with high elevation. Although strong surface heating enhances buoyancy and deepens the PBL, lower ambient temperatures reduce the lifting condensation level (LCL) for a given near-surface relative humidity, facilitating the frequent formation of low-level clouds (Wang et al., 2020). The combined effects of terrain-induced lifting, enhanced vertical moisture transport, and lower LCL contribute to the relatively low CBH over the Plateau.

CTH exhibits similar seasonal variability (Fig. S2), with mean values of 7.51 ± 1.00 km in summer, 6.37 ± 0.93 km in spring, 5.70 ± 0.71 km in autumn, and 4.70 ± 1.33 km in winter. The higher summer CTH reflects enhanced convective instability and stronger vertical development, whereas wintertime stability limits cloud growth largely to the lower troposphere. Regionally, CTH over the Tibetan Plateau is systematically lower than over eastern China. This finding is consistent with Chen et al. (2017), who reported that deep convective clouds over the Plateau are approximately 20–30% thinner than those over eastern China, and with Luo et al. (2011), who noted that convection over the Plateau is generally shallower and less frequent. The reduced vertical extent may be related to weaker large-scale dynamical forcing and frequent weak upward motion over the Plateau (Chen et al., 2017).

CT follows a seasonal cycle similar to that of CTH, with mean values of 3.56 ± 0.72 km in summer, 3.13 ± 0.49 km in spring, 2.93 ± 0.47 km in autumn, and 2.56 ± 0.72 km in winter (Fig. S3). The larger CT during summer reflects the combined effects of enhanced instability, deeper convective development,

https://doi.org/10.5194/egusphere-2026-1091
Preprint. Discussion started: 6 March 2026

and increased moisture availability, while the thinner winter clouds are consistent with suppressed vertical growth under stable atmospheric stratification.

3.3 Vertical distribution of cloud

Figure 5 presents the annual and seasonal mean vertical occurrence frequencies of CBH, CTH, and the combined cloud vertical profiles across China in 2024. These profiles provide insights into the climatological structures of clouds and the mechanisms governing their seasonal variability.

3.3.1 Vertical distribution of CBH

As shown in Fig. 5a, CBH occurrence frequency exhibits a pronounced unimodal distribution, with notable seasonal modulation. Across all seasons, the highest frequencies occur below 1 km, indicating the predominance of low-level cloud bases over continental China. This result is consistent with previous ground-based radar and lidar observations in mid-latitude continental regions, which document the frequent occurrence of low cloud bases in boundary-layer cloud regimes (e.g., Clothiaux et al., 2000; Wang and Sassen, 2001).

Distinct seasonal contrasts are evident. Above 6 km, CBH frequencies are highest in summer, whereas below 3.0 km, they peak in winter. This seasonal contrast reflects differences in thermodynamic instability, large-scale circulation, and the associated cloud types (Shupe et al., 2011). In summer, enhanced surface heating and abundant moisture supply associated with the East Asian summer monsoon promote deep boundary-layer development and vigorous convection, allowing cloud bases to form at higher altitudes, particularly for convective and high-level cloud systems (Ding and Chan, 2005; Mace et al., 2006). In winter, reduced insolation and colder temperatures lower the lifting condensation level (LCL) and suppress boundary-layer mixing. Moreover, the East Asian winter monsoon advects cold, dry air southward, strengthening static stability and limiting vertical development (Zhang et al., 1997). Under these conditions, condensation frequently occurs within shallow boundary layers, favouring low-base stratiform clouds such as stratus and stratocumulus (Klein and Hartmann, 1993).

3.3.2 Vertical distribution of CTH

In contrast to CBH, the vertical occurrence frequency of CTH exhibits a prominent bimodal distribution, with one peak occurring between 1.0 and 3.0 km and a second peak between 6 and 12 km (Fig. 5b). This bimodal pattern indicates the coexistence of two dominant cloud regimes over China: shallow low-topped clouds and deep convective or high-level cloud systems. The presence of both peaks reflects the diversity of synoptic environments and climatic regimes across the region.

https://doi.org/10.5194/egusphere-2026-1091
Preprint. Discussion started: 6 March 2026

The two modes exhibit distinct seasonal behavior. The high-altitude peak (6–12 km) is most pronounced in summer, particularly above 9 km. This enhancement is consistent with a deeper troposphere, stronger convective instability, and more frequent deep convection during the warm season. Intense surface heating combined with monsoonal moisture transport supports strong updrafts capable of transporting cloud tops into the upper troposphere (Johnson et al., 1999; Holloway and Neelin, 2009). In contrast, the low-altitude peak (1–3 km) dominates in winter, when stable stratification restricts vertical cloud growth and favours shallow stratiform cloud types (Klein and Hartmann, 1993; Wood and Bretherton, 2006).

3.3.3 Combined vertical cloud profiles

The combined vertical distribution derived from CBH and CTH (Fig. 5c) further illustrates seasonal contrasts in overall cloud depth. During summer, clouds occupy a broad vertical range, frequently extending from near the surface to above 9 km. This structure reflects the prevalence of deep convective systems supported by strong surface heating, enhanced instability, and abundant moisture supply (Houze, 2018). In winter, by contrast, cloud occurrence is largely confined below 6 km, and the vertical extent is substantially reduced. This shallow structure is consistent with the dominance of low-level stratiform clouds under cold, dry, and stable atmospheric conditions, where limited vertical mixing suppresses deep convection (Shupe et al., 2011; Pan et al., 2023).

3.4 Diurnal variation of cloud occurrence frequency at different heights

Compared with conventional radiosonde measurements, the MMCR provides much higher temporal resolution (1 min), enabling detailed characterization of the diurnal evolution of cloud vertical structure. Based on the retrieved CVS dataset, Figure 6 shows the annual mean diurnal variations of height-resolved cloud occurrence frequencies, along with the corresponding annual mean vertical profiles. Cloud occurrence frequencies were calculated at 1-hour intervals with a vertical resolution of 30 m, and the time refers to local time (LT).

3.4.1 Annual mean diurnal cycle

The annual mean diurnal variability extends primarily from 0.5 to 9 km, with the strongest fluctuations occurring below 3 km (Fig. 6b). Two prominent peaks in cloud occurrence frequency are identified: one in the morning (0600–0800 LT) and another in the afternoon (1400–1800 LT). These two peaks may be associated with seasonal influences. These peaks reflect the combined influence of nocturnal PBL processes and daytime convective development.

https://doi.org/10.5194/egusphere-2026-1091
Preprint. Discussion started: 6 March 2026

The morning peak is likely associated with nocturnal radiative cooling in the PBL, which enhances relative humidity and promotes the formation of low-level clouds under stable stratification. In contrast, the afternoon maximum corresponds to enhanced surface heating and increased boundary-layer instability, which favour convective cloud development. This diurnal pattern is broadly consistent with previous studies showing early-morning peaks in low cloud occurrence and late-afternoon maxima in convective activity (Li et al., 2008).

3.4.2 Seasonal modulation of the diurnal cycle

Figure 7 further shows seasonal mean diurnal variations in height-resolved cloud occurrence frequencies, along with the corresponding annual mean vertical profiles. The amplitude and vertical extent of diurnal variability differ markedly by season.

In summer (Fig. 7b), cloud occurrence variability spans a broad vertical range (approximately 1–10 km), substantially larger than in winter (Fig. 7d). This enhancement reflects the combined effects of strong surface heating and the East Asian summer monsoon (EASM). Enhanced solar radiation increases near-surface buoyancy and promotes vigorous convection, while monsoonal moisture transport provides the thermodynamic support necessary for deep cloud development. These conditions favour the frequent formation of deep convective clouds and produce pronounced diurnal variability extending into the upper troposphere (Houze, 2014; Wood, 2012).

The summer vertical profile exhibits a distinct two-layer structure. A lower layer (1–2 km) shows relatively weak diurnal variation, while an upper layer (3–9 km) displays a pronounced cycle. Within the upper layer, cloud occurrence reaches a minimum in the early morning (0600–0800 LT) and peaks in the late afternoon to early evening (1600–2000 LT). This pattern reflects the strong control of solar heating on convective instability: daytime heating destabilizes the planetary boundary layer, initiates moist convection, and drives the formation of cumuliform and deep convective clouds, leading to enhanced cloud occurrence in the afternoon (Betts, 2009; Zhang and Klein, 2013). At night, the absence of solar heating reduces convective turbulence and suppresses vertical moisture transport, thereby weakening upper-level cloud development.

In winter, the diurnal variability of cloud vertical distribution is considerably weaker and largely confined below 3 km. Cloud occurrence is most frequent between 0.5 and 3 km, consistent with the typical altitude range of liquid-phase stratiform clouds (Xu et al., 2023). A near-sunrise maximum (0600–0800 LT) is evident, in agreement with previous findings (Betts and Tawfik, 2016). This wintertime enhancement likely results from minimum near-surface air temperatures around sunrise under stable

https://doi.org/10.5194/egusphere-2026-1091
Preprint. Discussion started: 6 March 2026

boundary-layer conditions, which increase relative humidity and favour cloud formation (Dai, 2001; Eastman and Warren, 2014).

Spring and autumn exhibit transitional behavior between summer and winter. In spring (Fig. 7a), the vertical range of cloud variability expands relative to winter, with cloud tops occasionally reaching 7–8 km. An afternoon peak in mid-tropospheric cloud occurrence (3–6 km) is evident between 1400 and 1800 LT, reflecting strengthening solar heating and increasing convective instability. In autumn (Fig. 7c), cloud tops gradually lower and the diurnal amplitude weakens. Cloud occurrence becomes more evenly distributed throughout the day, particularly below 4 km, as solar radiation declines and atmospheric stratification strengthens. Overall, these transitional seasons illustrate the progressive adjustment of the cloud diurnal cycle to evolving surface heating and large-scale circulation, consistent with the broader seasonal evolution documented over China (Yu et al., 2007).

3.5 Impact of atmospheric thermodynamic factors on CVS

The vertical structure of clouds over China is regulated by a combination of thermodynamic stratification, moisture availability, and dynamical forcing. To quantify these controls, we examine the relationships between three key CVS metrics—CBH, CTH, and CT—and LTS, q_{850}, and WS_{700} using temporally and spatially collocated ERA5 reanalysis data. Across China, thermodynamic factors exert primary control on cloud vertical development, while dynamical forcing modulates cloud organization and geometric extent.

3.5.1 Cloud base height

Figure 8 displays the spatial distributions of correlation coefficients between CBH and three atmospheric variables. For the q_{850}, positive correlations dominate at 92.4% of stations (Fig. 8a). This widespread relationship indicates that environments with enhanced low-level moisture are generally associated with higher cloud bases in the climatological mean. Importantly, this positive correlation does not imply that moisture directly raises the lifting condensation level (LCL); rather, it reflects the co-variability of moisture and convective instability. Under moist and unstable conditions, deeper PBL development and stronger updrafts elevate cloud bases, particularly for cumuliform and convective cloud regimes (Betts, 2004; Zhang and Klein, 2013). This relationship is statistically robust and spatially coherent, particularly over southern China and the eastern margins of the Tibetan Plateau, where moist convection frequently regulates cloud vertical development.

https://doi.org/10.5194/egusphere-2026-1091
Preprint. Discussion started: 6 March 2026

The few negative correlations (7.6%), scattered over arid northwestern China, likely reflect the dominance of large-scale subsidence, which decouples local moisture variability from cloud formation (Riemann-Campe et al., 2011).

In contrast, CBH exhibits predominantly negative correlations with LTS (72.5% of stations; Fig. 8b), most notably over southeastern coastal China and the Sichuan Basin. Higher LTS indicates stronger lower-tropospheric stratification, which suppresses boundary-layer growth and favours shallow stratiform clouds with lower bases (Klein and Hartmann, 1993; Wood and Bretherton, 2006). Conversely, reduced LTS enhances instability, promotes deeper turbulent mixing, and supports the development of higher cloud bases associated with convective clouds (Slingo, 2007).

Positive correlations (27.5%), primarily over the Tibetan Plateau and parts of northern China, likely arise in regions where LTS variations are coupled with large-scale dynamical lifting or orographic forcing, complicating the direct stability–CBH relationship (Medeiros et al., 2010).

In contrast, CBH exhibits no coherent national-scale relationship with WS_{700} (Fig. 8c), with nearly equal proportions of positive (52.2%) and negative (47.8%) correlations. This near-symmetric distribution suggests that vertical wind shear exerts a context-dependent influence on CBH (Jiang et al., 2012). In some regions (e.g., northern China), stronger shear may enhance convective organization and elevate inflow layers, leading to higher cloud bases (Weisman and Rotunno, 2000). In others (e.g., southern China), shear-enhanced mixing and low-level convergence may promote lower cloud bases (Houze, 2018). Overall, the absence of a uniform signal indicates that dynamical shear does not systematically control CBH at the national scale.

3.5.2 Cloud top height

Cloud top height exhibits broadly similar but more pronounced thermodynamic sensitivity (Fig. 9). For q_{850} (Fig. 9a), positive correlations dominate across 96.3% of stations, indicating that abundant low-level moisture sustains buoyant ascent and supports deeper cloud development. This relationship is most pronounced over southern China and the eastern Tibetan Plateau margins, where active moist convection prevails. Higher specific humidity provides ample moisture supply to convective systems, enabling air parcels to maintain positive buoyancy over deeper layers and reach higher levels before encountering their level of neutral buoyancy (Johnson et al., 1999; Holloway and Neelin, 2009). The few negative correlations (3.7%), scattered over arid northwestern China, likely reflect the dominance of large-scale subsidence that inhibits deep convective development regardless of local moisture availability (Riemann-Campe et al., 2011).

https://doi.org/10.5194/egusphere-2026-1091
Preprint. Discussion started: 6 March 2026

CTH is predominantly negatively correlated with LTS (65.8% of stations; Fig. 9b), particularly over coastal southeastern China, the Sichuan Basin, and the Yangtze River valley. The explanation parallels that for CTH: higher LTS suppresses vertical cloud growth, favouring shallow cloud formations with lower cloud tops (Klein and Hartmann, 1993; Wood and Bretherton, 2006), while lower LTS enables vigorous deep convective development that extends to higher altitudes (Slingo, 1987). Positive correlations (34.2% of stations), primarily over the Tibetan Plateau and parts of northern China, may reflect situations where LTS variations are coupled with large-scale dynamical lifting or orographic forcing (Medeiros et al., 2010).

By comparison, CTH shows a predominantly negative correlation with WS_{700} (69.6% of stations; Fig. 9c), with negative correlations concentrated over southern China, the Tibetan Plateau margins, and northeastern China. This pattern indicates that stronger vertical wind shear tends to suppress vertical cloud development, thereby lowering cloud top heights. Several mechanisms may explain this relationship: (1) Enhanced entrainment mixing near cloud edges, which dilutes buoyancy and limits vertical growth; (2) Disruption of vertically coherent updrafts during early convective stages; and (3) Increased upper-level turbulence that spreads anvils horizontally rather than vertically (Sathiyamoorthy et al., 2004). These processes reduce maximum cloud-top altitude and favour layered cloud structures (Yang et al., 2022).

Positive correlations (30.4%), scattered mainly over northwestern China, may reflect environments where moderate shear organizes convection into longer-lived systems capable of deeper vertical development—consistent with the "optimal shear" framework (Weisman and Rotunno, 2000).

3.5.3 Cloud thickness

Cloud thickness exhibits distinct correlation patterns that differ from those of CBH and CTH (Fig. 10). For q_{850} (Fig. 10a), positive correlations dominate across 67.5% of stations, indicating that abundant low-level moisture favours vertically extended clouds. This relationship is pronounced over southern China and the eastern Tibetan Plateau margins, where active moist convection prevails. Higher specific humidity sustains positive buoyancy over deeper layers, promoting thicker clouds (Johnson et al., 1999; Holloway and Neelin, 2009). Negative correlations (32.5% of stations), scattered over arid northwestern China and parts of Inner Mongolia, may reflect environments where moisture is insufficient to support deep convective development, or where enhanced low-level moisture triggers early precipitation that limits further vertical growth.

For LTS (Fig. 10b), cloud thickness exhibits a predominantly positive correlation (67.1% of stations), concentrated over southern China, the Sichuan Basin, and the Yangtze River valley. This contrasts with the negative LTS correlations observed for CBH and CTH. The positive relationship arises

https://doi.org/10.5194/egusphere-2026-1091
Preprint. Discussion started: 6 March 2026

because moderate to high LTS is often associated with stratiform cloud regimes, which, while having limited vertical extent individually, can develop considerable geometric thickness through layered cloud structures and persistent moisture supply (Klein and Hartmann, 1993; Wood and Bretherton, 2006). Negative correlations (32.9% of stations), primarily over the Tibetan Plateau and parts of northern China, reflect situations where low LTS enhances atmospheric instability and promotes deep convection, but the resulting clouds exhibit highly variable thickness depending on convective stage and precipitation processes (Slingo, 1987; Medeiros et al., 2010).

Cloud thickness shows a predominantly negative correlation with WS_{700} (78.3% of stations; Fig. 10c), with negative correlations widespread across southern China, the Tibetan Plateau margins, northeastern China, and the North China Plain. This strong negative relationship indicates that stronger vertical wind shear suppresses vertical cloud development, reducing cloud thickness. Multiple mechanisms operate across different atmospheric layers. Large-eddy simulations demonstrate that vertical wind shear—particularly backward shear (surface easterlies becoming upper westerlies)—limits vertical cloud development in trade-wind cumulus convection, leading to shallower cloud layers (Helfer et al., 2020). Wind shear across the cloud-top interface enhances entrainment mixing and turbulent kinetic energy production, diluting cloud cores and suppressing vertical growth (Mellado and Stevens, 2014). Strong upper-level shear limits upward deep convective development by enhancing turbulence over cloud tops and extending anvils horizontally (Sathiyamoorthy et al., 2004) and disrupts organized updraft structures (Bi et al., 2023). Positive correlations (21.7% of stations), scattered across limited areas of northwestern China, may reflect environments where moderate shear organizes convection into longer-lived systems that achieve greater vertical development through enhanced moisture convergence—consistent with the concept of "optimal" shear for organized deep convection (Weisman and Rotunno, 2000).

3.6 Joint thermodynamic-dynamic controls

Because atmospheric controls rarely operate in isolation, we further examine the joint regulation of CVS by paired thermodynamic and dynamical variables. This bivariate analysis reveals that moisture availability establishes the fundamental precondition for vertical cloud development, while instability and wind shear determine the efficiency with which that moisture is converted into vertical growth. Under high-humidity and low-LTS conditions, clouds attain maximum CBH, CTH, and CT. In contrast, high LTS suppresses vertical development regardless of moisture or shear intensity, demonstrating the dominant stabilizing control of stratification. Wind shear exhibits a nonlinear influence: moderate shear enhances convective organization under unstable conditions, whereas strong shear inhibits vertical cloud

https://doi.org/10.5194/egusphere-2026-1091
Preprint. Discussion started: 6 March 2026

growth through enhanced mixing. This joint dependence confirms that thermodynamic forcing provides the primary control on CVS across China, with dynamical processes acting as modulators.

3.6.1 Cloud base height

Figure 11 illustrates the joint dependence of CBH on paired atmospheric variables. For the q_{850}–LTS combination (Fig. 11a), CBH generally increases with q_{850}, but the sensitivity depends strongly on stability. Under low LTS (unstable) conditions, CBH reaches its highest values when moisture is abundant, consistent with environments favouring deep boundary-layer development and convective cloud regimes. Under high LTS (stable) conditions, CBH remains low across nearly all humidity bins, indicating that strong stratification limits boundary-layer growth and favours low-base stratiform clouds regardless of moisture availability.

The LTS–WS_{700} relationship (Fig. 11b) further demonstrates this conditional behavior. Under low LTS, CBH tends to increase with increasing shear, consistent with the role of shear in organizing convection and modulating inflow structure in unstable environments (Weisman and Rotunno, 2000). Under high LTS, CBH remains uniformly low and exhibits weak sensitivity to shear, again emphasizing that stability constrains cloud-base variability.

For the q_{850} – WS_{700} pairing (Fig. 11c), CBH increases primarily with q_{850}, while shear acts as a secondary modulator. The largest CBH values occur when high moisture coincides with moderate-to-strong shear, suggesting that organized convection and enhanced mixing in such environments can support higher cloud bases. When q_{850} is low, increasing shear alone produces only limited increases in CBH, indicating that moisture availability remains a prerequisite for elevated cloud bases.

3.6.2 Cloud top height

The joint dependence of CTH on paired variables (Fig. 12) is broadly consistent with that of CBH, but with greater sensitivity to deep-convective environments. For the q_{850}–LTS combination (Fig. 12a), CTH maximizes under high humidity and low LTS, consistent with vigorous vertical development supported by strong buoyancy and ample moisture supply (Johnson et al., 1999). Compared with CBH, the dependence of CTH on humidity under unstable conditions is more gradual, indicating that processes aloft—such as entrainment, detrainment, and upper-level thermodynamic structure—also influence maximum cloud-top altitude.

The LTS–WS_{700} pairing (Fig. 12b) indicates that CTH is largest under low LTS with moderate-to-strong shear, consistent with the concept of “optimal shear” conditions that favour organized deep

https://doi.org/10.5194/egusphere-2026-1091
Preprint. Discussion started: 6 March 2026

convection (Weisman and Rotunno, 2000). Under high LTS, CTH remains low across all shear bins, reaffirming that stable stratification suppresses vertical development irrespective of dynamical forcing. For the q_{850}–WS_{700} combination (Fig. 12c), CTH increases with both humidity and shear, with the highest values occurring when high q_{850} coincides with strong shear. This behaviour is consistent with shear-enhanced convective organization when sufficient moisture is available, whereas under low humidity, increasing shear alone does not substantially elevate cloud tops.

3.6.3 Cloud thickness

Cloud thickness exhibits distinct joint-dependence characteristics (Fig. 13), reflecting its integrated sensitivity to both cloud-base and cloud-top processes. For the q_{850}–LTS combination (Fig. 13a), the thickest clouds occur under high humidity and low LTS. CT shows a particularly strong dependence on stability when humidity is high, indicating that instability is critical for realizing large vertical extent once moisture requirements are satisfied.

The LTS–WS_{700} relationship (Fig. 13b) shows that maximum CT tends to occur under low LTS with moderate shear. In contrast, strong shear under unstable conditions is associated with reduced CT, consistent with the dual role of shear: moderate shear can enhance organization, whereas excessive shear increases entrainment mixing and promotes detrainment that limits net cloud depth (Mellado and Stevens, 2014; Helfer et al., 2020). Under high LTS, CT remains uniformly small and exhibits weak sensitivity to shear, again indicating that stability strongly constrains vertical development.

For the q_{850}–WS_{700} combination (Fig. 13c), CT increases primarily with q_{850}, while shear influences CT more strongly under high-humidity conditions. When humidity is low, CT remains limited across all shear bins; when humidity is high, CT increases with shear up to moderate–strong values. These joint results further support the view that moisture availability is a necessary precondition for substantial cloud depth, while wind shear regulates the realized vertical extent by modulating organization and mixing.

3.7 The land surface modulation of cloud vertical structure

In addition to atmospheric thermal and dynamical factors, the vertical structure of clouds is influenced by underlying land-surface characteristics through their effects on PBL moisture, surface energy partitioning, and turbulence (e.g., Bonan, 2008; Fu et al., 2020; Wang et al., 2021). Because CBH is closely linked to PBL thermodynamics, it provides a useful metric for assessing surface–cloud coupling. To quantify land-surface influences, we compare CBH across land cover types under two conditions: (i) all clouds and (ii) afternoon single-layer clouds (Fig. 14), which are expected to exhibit stronger coupling to surface forcing during peak daytime heating.

https://doi.org/10.5194/egusphere-2026-1091
Preprint. Discussion started: 6 March 2026

3.7.1 All-cloud conditions

Under all-cloud conditions, CBH exhibits substantial variability across land cover types, with interquartile ranges typically spanning approximately 1–6 km (Fig. 14). Barren land (type 10) shows the highest median CBH, consistent with limited surface moisture availability and a tendency toward higher lifting condensation levels and fewer low-base clouds. In contrast, vegetated surfaces (types 2–7) generally exhibit lower median CBH. Among these, evergreen broadleaf forest (type 2) and deciduous broadleaf forest (type 3) show the lowest median CBH, while grasslands (type 6) and croplands (type 7) display moderately low values.

These contrasts can be interpreted in terms of land-cover biophysical properties. Forested regions typically sustain higher evapotranspiration, increasing boundary-layer moisture and supporting moisture recycling (Spracklen et al., 2012; Zhang et al., 2024). In addition, lower canopy albedo and greater surface roughness can enhance turbulent exchange, influencing boundary-layer growth and cloud formation. Collectively, these mechanisms favour cloud formation and can contribute to lower cloud bases over forests relative to sparsely vegetated or barren surfaces. This interpretation is consistent with observational and modeling studies demonstrating that land-use and land-cover change can modify CBH by altering the partitioning between sensible and latent heat fluxes and the resulting boundary-layer thermodynamics (Syktus and McAlpine, 2016; Xu et al., 2022; Duveiller et al., 2023).

3.7.1 Afternoon single-layer clouds

Afternoon single-layer clouds show an even clearer dependence of CBH on land cover type. As in the all-cloud case, the highest median CBH occurs over barren land (type 10), while the lowest median values are found over evergreen and deciduous broadleaf forests (types 2 and 3). Notably, the median CBH for afternoon single-layer clouds is systematically higher than for all clouds by ~41.5% on average, and the land-cover contrasts are amplified. For example, CBH over barren land is ~20.0% higher for afternoon single-layer clouds than under all-cloud conditions. Over evergreen broadleaf forest (type 2) and deciduous broadleaf forest (type 3), the corresponding increases are ~36.4% and ~55.9%, respectively.

Two factors likely contribute to these systematic differences. First, single-layer cloud regimes often occur under relatively dry or weakly forced conditions, which can be associated with higher condensation levels than multi-layer or deep convective regimes. Second, peak daytime heating in the afternoon deepens the boundary layer and can raise cloud bases through enhanced turbulent mixing and increased boundary-layer temperature. The amplified land-cover contrasts during afternoon hours may also reflect enhanced sensitivity of boundary-layer evolution to surface heterogeneity under strong insolation.

https://doi.org/10.5194/egusphere-2026-1091
Preprint. Discussion started: 6 March 2026

Heterogeneous landscapes can generate mesoscale circulations and spatial gradients in moisture and heat fluxes that modulate cloud initiation and cloud-base height (Rieck et al., 2014).

Overall, Fig. 14 demonstrates that land cover type exerts a measurable influence on CBH, with the strongest contrasts emerging for afternoon single-layer clouds. These results underscore the importance of surface-driven moisture supply, energy partitioning, and boundary-layer dynamics in shaping cloud-base variability. Similar forest–open land contrasts in CBH have been reported in other regions (e.g., tropical montane environments using distributed sensor networks; Trivedi et al., 2025), suggesting that land-surface modulation of cloud vertical structure may be a robust feature across diverse geographic settings.

4. Summary and concluding remarks

This study presents the first national-scale, high-spatiotemporal-resolution characterization of cloud vertical structure (CVS) across China based on observations from a coordinated network of 80 Ka-band cloud radars. The dataset provides unprecedented detail—30 m vertical and 1 min temporal resolution—enabling a comprehensive investigation of the spatial distribution, seasonal evolution, diurnal variability, and governing controls of cloud vertical structure. Our results demonstrate pronounced spatial, seasonal, and diurnal variability in CVS, reflecting strong modulation by monsoonal circulation, thermodynamic stratification, and regional terrain.

The national annual mean cloud occurrence frequency is 56.7%, with single-layer clouds dominating (34.7%), followed by two-layer (14.7%) and multi-layer clouds (7.1%). Spatially, single-layer clouds are more prevalent over arid northwestern China, whereas multi-layer clouds occur more frequently in humid southeastern regions. This striking contrast highlights the regulatory role of moisture availability and atmospheric instability in shaping cloud vertical complexity.

Cloud height exhibits clear seasonal modulation. CBH follows the order of summer > spring > autumn > winter, consistent with seasonal variations in solar heating and boundary-layer development. The Tibetan Plateau shows systematically lower CBH in spring and summer, reflecting the combined influence of lower ambient temperatures, terrain-induced lifting, and unique boundary-layer thermodynamics. Vertically, CBH displays a unimodal distribution dominated by low-level clouds, whereas CTH exhibits a bimodal structure, indicating the coexistence of shallow stratiform and deep convective cloud regimes across China.

Diurnal variations in CVS are strongly seasonally dependent. In summer, upper-level cloud occurrence (3–9 km) peaks during the late afternoon (1600–2000 LT), driven by enhanced surface heating and convective instability. In winter, clouds are largely confined below 3 km and exhibit a near-sunrise

https://doi.org/10.5194/egusphere-2026-1091
Preprint. Discussion started: 6 March 2026

maximum (0600–0800 LT), consistent with nocturnal radiative cooling and stable boundary-layer conditions. Spring and autumn display transitional behaviour between these two regimes.

Thermodynamic conditions exert the dominant control on CVS across China. Both CBH and CTH are positively correlated with the specific humidity at 850 hPa (q_{850}) and negatively correlated with the lower-tropospheric stability (LTS), indicating that abundant moisture and reduced atmospheric stability favor the vertical development of clouds. The wind shear at 700 hPa (WS_{700}) plays a secondary but systematic role: CTH and cloud thickness (CT) are predominantly negatively correlated with WS_{700}, suggesting that strong wind shear suppresses vertical cloud growth by enhancing entrainment and disrupting organized updrafts. Joint analyses further reveal that high humidity combined with low LTS maximizes cloud vertical development, whereas high LTS constrains CVS regardless of moisture availability or wind shear magnitude. Wind shear exhibits nonlinear impacts on CVS: moderate shear occasionally supports organized convection under unstable thermodynamic conditions, but strong shear generally limits the vertical extent of cloud systems.

Land cover type exerts a measurable influence on CBH, particularly for afternoon single-layer clouds. The median CBH of afternoon single-layer clouds is approximately 41.5% higher than that under all-cloud conditions, reflecting enhanced PBL growth during peak daytime solar heating. Among different land cover types, barren lands exhibit the highest CBH, likely due to the limited surface moisture supply and weak evapotranspiration. In contrast, forested regions display the lowest CBH, consistent with enhanced evapotranspiration, moisture recycling, and strong land–atmosphere coupling. The largest relative enhancement in afternoon CBH is observed over deciduous broadleaf forests (+55.9%), underscoring the amplification of land–atmosphere feedback processes under strong solar forcing.

Overall, this study provides a high-resolution, observationally constrained dataset of CVS across China and establishes a quantitative framework linking CVS to its thermodynamic, dynamical, and land-surface controls (schematically summarized in Fig. 15). These findings offer valuable observational constraints for evaluating and improving cloud parameterization schemes in numerical weather prediction (NWP) and climate models—critical for reducing uncertainties in simulating regional precipitation, energy balance, and climate feedbacks over China. Future work should extend this analysis to multi-year observational datasets to quantify the interannual variability of CVS and explore its role in extreme weather events (e.g., heavy rainfall, heatwaves) and regional climate feedback mechanisms.

Code/Data availability. The authors would like to acknowledge the National Meteorological Information Centre (NMIC) of CMA (http://data.cma.cn/en, CMA, 2024) for providing the Ka-band millimeter-wave

https://doi.org/10.5194/egusphere-2026-1091
Preprint. Discussion started: 6 March 2026

cloud radar (MMCR) data and radar wind profiler (RWP) data, and the ECMWF for providing ERA5 reanalysis data (Hersbach et al., 2020).

Author contribution. JG conceptualized this study. HX, JG, and JD carried out the analysis with comments from other co-authors. HX wrote the paper with contribution from JG, RY, DM, JZ, JC, NL, LZ, YZ, and TC provided useful suggestions for the study. BT contributed to the big data analysis. All authors contributed to the improvement of paper.

Competing interests. The contact author has declared that none of the authors has any competing interests.

Acknowledgments. The authors would like to acknowledge the National Meteorological Information Centre (NMIC) of CMA for providing Ka-band millimeter-wave cloud radar (MMCR) data. We would also like to thank the CMA for radar wind profiler (RWP) data, and the ECMWF for ERA5 data.

Financial support. This work was jointly supported by the National Natural Science Foundation of China (NSFC) under grants 42325501, 42561160141, and 42505135, Department of Science and Technology of Guizhou under grant KXJZ [2024] 033, the Science and Technology Supporting Project of Guizhou Province ([2023]236, and the Chinese Academy of Meteorological Sciences under grant 2024Z003.

References

An, N., Pinker, R. T., Wang, K., Rogers, E., and Zuo, Z.: Evaluation of cloud base height in the North American regional reanalysis using ceilometer observations, *Int. J. Climatol.*, 40 (6), 3161–3178, https://doi.org/10.1002/joc.6389, 2019.

Betts, A. K.: Understanding hydrometeorology using global models, *Bull. Amer. Meteor. Soc.*, 85 (11), 1673–1688, https://doi.org/10.1175/BAMS-85-11-1673, 2004.

Betts, A. K.: Land-surface-atmosphere coupling in observations and models, *J. Adv. Model Earth Syst.*, 1 (3), 4, https://doi.org/10.3894/JAMES.2009.1.4, 2009.

Betts, A. K., and Tawfik, A. B.: Annual climatology of the diurnal cycle on the Canadian Prairies, *Front. Earth Sci.*, 4, 1, https://doi.org/10.3389/feart.2016.00001, 2016.

Bi, M. Y., Wang, R. F., Li, T. M., and Ge, X. Y.: Effects of vertical shear on intensification of tropical cyclones of different initial sizes, *Front. Earth Sci.*, 11, 1106204, https://doi.org/10.3389/feart.2023.1106204, 2023.

https://doi.org/10.5194/egusphere-2026-1091
Preprint. Discussion started: 6 March 2026

779 Bonan, G. B.: Forests and climate change: Forcings, feedbacks, and the climate benefits of forests,
780 *Science*, 320 (5882), 1444–1449, https://doi.org/10.1126/science.1155121, 2008.
781 Bony, S., Stevens, B., Frierson, D. M. W., Jakob, C., Kageyama, M., Pincus, R., Shepherd, T. G.,
782 Sherwood, S. C., Siebesma, A. P., and Sobel, A. H.: Clouds, circulation and climate sensitivity, *Nat.*
783 *Geosci*, 8, 261–268, https://doi.org/10.1038/NGEO2398, 2015.
784 Cesana, G. and Waliser, D. E., Characterizing and understanding systematic biases in the vertical structure
785 of clouds in CMIP5/CFMIP2 models, *Geophys. Res. Lett.*, 43 (19), 10538–10546,
786 https://doi.org/10.1002/2016GL070515, 2016.
787 Cesana, G. V., Khadir, T., Chepfer, H., and Chiriaco, M.: Southern ocean solar reflection biases in CMIP6
788 models linked to cloud phase and vertical structure representations, *Geophys. Res. Lett.*, 49 (22),
789 e2022GL099777, https://doi.org/ 10.1029/2022GL099777, 2022.
790 Chae, J. H., and Sherwood, S. C.: Insights into cloud-top height and dynamics from the seasonal cycle of
791 cloud-top heights observed by MISR in the West Pacific region, *J. Atmos. Sci.*, 67, 248–261,
792 https://doi.org/10.1175/2009JAS3099.1, 2010.
793 Chen, D, Guo, J., Yao, D., Lin, Y., Zhao, C., Min, M., Xu, H., Liu, L., Huang, X., Chen, T., and Zhai, P.:
794 Mesoscale convective systems in East Asia from Advanced Himawari Imager: Algorithms and
795 preliminary results, *J. Geophys. Res. Atmos.,* 124, 2210–2234,
796 https://doi.org/10.1029/2018JD029707, 2019.
797 Chen, J. H., Wu, X. Q., Yin, Y., Huang, Q., and Xiao, H.: Characteristics of cloud systems over the
798 Tibetan Plateau and East China during boreal summer, *J. Clim.*, 30 (9), 3117–3137,
799 https://doi.org/10.1175/JCLI-D-16-0169.1, 2017.
800 Chen, P., Yang, L. M., Zeng, Y., Tong, Z. P., and Jiang, Y. F.: Fine vertical structures of cloud from a
801 ground-based cloud radar over the western Tianshan mountains, *Meteorol. Appl.*, 29 (6), e2105,
802 https://doi.org/10.1002/met.2105, 2022.
803 Chen, Q., Fan, J., Hagos, S., Gustafson Jr., W. I., and Berg, L. K.: Roles of wind shear at different vertical
804 levels: Cloud system organization and properties, *J. Geophys. Res.-Atmos.*, 120, 6551–6574,
805 https://doi.org/10.1002/2015JD023253, 2015.
806 Chi, Y. L., Zhao, C. F., Yang, Y. K., Ma, Z. S., and Yang, J.: Cloud macrophysical characteristics in
807 China mainland and east coast from 2006 to 2017 using satellite active remote sensing observations,
808 *Int. J. Climatol.*, 42 (16), 8984–9002, https://doi.org/10.1002/joc.7790, 2022.
809 Clothiaux, E. E., Moran, K. P., Martner, B. E., Ackerman, T. P., Mace, G. G., Uttal, T., Mather, J. H.,
810 Widener, K. B., Miller, M. A., and Rodriguez, D. J.: The atmospheric radiation measurement

https://doi.org/10.5194/egusphere-2026-1091
Preprint. Discussion started: 6 March 2026

program cloud radars: Operational modes, *J. Atmos. Oceanic Technol.*, 16 (7), 819–827, https://doi.org/10.1175/15200426(1999)016<0819:TARMPC>2.0.CO;2, 1999.

Clothiaux, E. E., Ackerman, T. P., Mace, G. G., Moran, K. P., Marchand, R. T., Miller, M. A., and Martner, B. E.: Objective determination of cloud heights and radar reflectivities using a combination of active remote sensors at the ARM CART sites, *J. Appl. Meteorol.*, 39, 645–665, https://doi.org/10.1175/15200450(2000)039<0645:odocha>2.0.co;2, 2000.

Dai, A. G.: The diurnal cycle from observations and ERA5 in surface pressure, temperature, humidity, and winds, *Clim. Dyn.*, 61 (5–6), 2965–2990, https://doi.org/10.1007/s00382-023-06721-x, 2023.

Das, S. K., Uma, K. N., Konwar, M., Raj, P. E., Deshpande, S. M., and Kalapureddy, M. C. R.: CloudSat-CALIPSO characterizations of cloud during the active and the break periods of Indian summer monsoon, *J. Atmos. Solar-Terr. Phys.*, 97, 106–114, https://doi.org/10.1016/j.jastp.2013.02.016, 2013.

Ding, Y., and Chan, J. C. L.: The East Asian summer monsoon: An overview, *Meteor. Atmos. Phys.*, 89, 117–142, https://doi.org/10.1007/s00703-005-0125-z, 2005.

Duveiller, G., Filipponi, F., Ceglar, A., Bojanowski, J., Alkama, R., and Cescatti, A.: Revealing the widespread potential of forests to increase low level cloud cover, *Nat. Commun.*, 12 (1), 4337, https://doi.org/10.1038/s41467-021-24551-5, 2021.

Eirund, G. K., Possner, A., and Lohmann, U.: The impact of warm and moist airmass perturbations on Arctic mixed-phase stratocumulus, *J. Clim.*, 33 (22), 9615–9628, https://doi.org/10.1175/JCLI-D-20-0163.1, 2021.

Fan, J., Wu, L., Zhang, F., Xiang, Y., and Zheng, J.: Climate change effects on reference crop evapotranspiration across different climatic zones of China during 1956–2015, *J. Hydrol.*, 542, 923–937, https://doi.org/10.1016/j.jhydrol.2016.09.060, 2016.

Fang, J. J., Huang, K. M., Du, M. K., Zhang, Z. R., Cao, R., and Yi, F.: Investigation on cloud vertical structures based on Ka-band cloud radar observations at Wuhan in Central China, *Atmos. Res.*, 281, 106492, https://doi.org/10.1016/j.atmosres.2022.106492, 2023.

Feng, Y., Jia, Y., Zhang, Q., Gong, D., and Cui, N.: National-scale assessment of pan evaporation models across different climatic zones of China, *J. Hydrol.*, 564, 314–328, https://doi.org/10.1016/j.jhydrol.2018.07.013, 2018.

Frank, W. M., and Ritchie, E. A.: Effects of vertical wind shear on the intensity and structure of numerically simulated hurricanes, *Mon. Wea. Rev.*, 129 (9), 2249 – 2269, https://doi.org/10.1175/1520-0493(2001)129<2249:EOVWSO>2.0.CO;2, 2001.

https://doi.org/10.5194/egusphere-2026-1091
Preprint. Discussion started: 6 March 2026

Fu, Y. F., Ma, Y. M., Zhong, L., Yang, Y. J., Guo, X. L., and Wang, C. H., Xu, X. F., Yang, K., Xu, X. D., Liu, L. P., Fan, G. Z., Li, Y. Q., and Wang, D. H.: Land-surface processes and summer-cloud-precipitation characteristics in the Tibetan Plateau and their effects on downstream weather: A review and perspective, *Natl. Sci. Rev.*, 7 (3), 500–515, https://doi.org/10.1093/nsr/nwz226, 2020.

George, G., Sarangi, C., Tripathi, S. N., Chakraborty, T., and Turner, A.: Vertical structure and radiative forcing of monsoon clouds over Kanpur during the 2016 INCOMPASS field campaign, *J. Geophys. Res.–Atmos.*, 123 (4), 2152–2174, https://doi.org/10.1002/2017JD027759, 2018.

Helfer, K. C., Nuijens, L., de Roode, S. R., and Siebesma, A. P.: How wind shear affects trade-wind cumulus convection, *J. Adv. Model. Earth Syst.*, 12, e2020MS002183, https://doi.org/10.1029/2020MS002183, 2020.

Hersbach, H., Bell, B., Berrisford, P., Hirahara, S., Horányi, A., Muñoz-Sabater, J., Nicolas, J., Peubey, C., Radu, R., Schepers, D., Simmons, A., Soci, C., Abdalla, S., Abellan, X., Balsamo, G., Bechtold, P., Biavati, G., Bidlot, J., Bonavita, M., Chiara, G., Dahlgren, P., Dee, D., Diamantakis, M., Dragani, R., Flemming, J., Forbes, R., Fuentes, M., Geer, A., Haimberger, L., Healy, S., Hogan, R.J., Hólm, E., Janisková, M., Keeley, S., Laloyaux, P., Lopez, P., Lupu, C., Radnoti, G., Rosnay, P., Rozum, I., Vamborg, F., Villaume, S., and Thépaut, J-N.: The ERA5 global reanalysis, *Q.J.R. Meteorol. Soc.*, 146, 1999–2049, https://doi.org/10.1002/qj.3803, 2020.

Huang, J., J. Guo, F. Wang, Z. Liu, M. -J. Jeong, H. Yu and Z. Zhang: CALIPSO inferred most probable heights of global dust and smoke layers, *Journal of Geophysical Research-Atmospheres*, 120 (10), 5085–5100, https://doi.org/10.1002/2014JD022898, 2015.

Holloway, C. E., and Neelin, J. D.: Moisture vertical structure, column water vapor, and tropical deep convection, *J. Atmos. Sci.*, 66 (6), 1665–1683, https://doi.org/10.1175/2008JAS2806.1, 2009.

Houze, R. A., and Robert, A.: Cloud Dynamics, 2nd ed., Academic Press, 432 pp., ISBN 9780123742667, 2018.

IPCC (2021). Summary for Policymakers, in: Climate Change 2021: The Physical Science Basis. Contribution of Working Group I to the Sixth Assessment Report of the Intergovernmental Panel on Climate Change, edited by: Masson-Delmotte, V., Zhai, P., Pirani, A., Connors, S. L., Péan, C., Berger, S., Caud, N., Chen, Y., Goldfarb, L., Gomis, M. I., Huang, M., Leitzell, K., Lonnoy, E., Matthews, J. B. R., Maycock, T. K., Waterfield, T., Yelekçi, O., Yu, R. and Zhou, B., Cambridge University Press.

Jiang, J. H., Su, H., Zhai, C. X., Perun, V. S., Del Genio, A., Nazarenko, L. S., Donner, L. J., Horowitz, L., Seman, C., Cole, J., Gettelman, A., Ringer, M. A., Rotstayn, L., Jeffrey, S., Wu, T. W., Brient, F., Dufresne, J. L., Kawai, H., Koshiro, T., Watanabe, M., LÉcuyer, T. S., Volodin, E. M., Iversen,

https://doi.org/10.5194/egusphere-2026-1091
Preprint. Discussion started: 6 March 2026

T., Drange, H., Mesquita, M. D. S., Read, W. G., Waters, J. W., Tian, B. J., Teixeira, J., and Stephens, G. L.: Evaluation of cloud and water vapor simulations in CMIP5 climate models using NASA "A-Train" satellite observations, *J. Geophys. Res. Atmos.*, 117, D14105, https://doi.org/10.1029/2011JD017237, 2012.

Johnson, R. H., Rickenbach, T. M., Rutledge, S. A., Ciesielski, P. E., and Schubert, W. H.: Trimodal characteristics of tropical convection, *J. Clim.*, 12, 2397–2418, https://doi.org/10.1175/1520-0442(1999)012<2397:TCOTC>2.0.CO;2, 1999.

Kalapureddy, M. C. R., Sukanya, P., Das, S. K., Deshpande, S. M., Pandithurai, G., Pazamany, A. L., Ambuj, K. J., Chakravarty, K., Kalekar, P., and Devisetty, H. K.: A simple biota removal algorithm for 35 GHz cloud radar measurements, *Atmos. Measure. Tech.*, 11, 1417–1436, https://doi.org/10.5194/amt-11-1417-2018, 2018.

Klein, S. A., and Hartmann, D. L.: The seasonal cycle of low stratiform clouds, *J. Clim.*, 6, 1587–1606, https://doi.org/10.1175/1520-0442(1993)006<1587:TSCOLS>2.0.CO;2, 1993.

Kollias, E., Clothiaux, E., Miller, M. A., Albrecht, B. A., Stephens, G. L., and Ackerman, T. P.: Millimeter-wavelength radars– New frontier in atmospheric cloud and precipitation research, *B. Am. Meteorol. Soc.*, 88, 1608–1624, https://doi.org/10.1175/bams88-10-1608, 2007.

Konsta, D., Dufresne, J. L., Chepfer, H., Vial, J., Koshiro, T., Kawai, H., Bodas-Salcedo, A., Roehrig, R., Watanabe, M., and Ogura, T.: Low-level marine tropical clouds in six CMIP6 models are too few, too bright but also too compact and too homogeneous, *Geophys. Res. Lett.*, 49, e2021GL097593, https://doi.org/10.1029/2021GL097593, 2022.

Li, J., Lv, Q., Jian, B., Zhang, M., Zhao, C., Fu, Q., Kawamoto, K., and Zhang, H.: The impact of atmospheric stability and wind shear on vertical cloud overlap over the Tibetan Plateau, *Atmos. Chem. Phys.*, 18 (10), 7329–7343, https://doi.org/10.5194/acp-18-7329-2018, 2018.

Li, Y. X., Yi, B. Q., and Min, M.: Diurnal variations of cloud optical properties during day-time over China based on Himawari-8 satellite retrievals, *Atmos. Environ.*, 277, 119065, https://doi.org/10.1016/j.atmosenv.2022.119065, 2022.

Li, Y., Yu, R., Xu, Y., and Zhang, X.: Spatial distribution and seasonal variation of cloud over China based on ISCCP data and surface observations, *J. Meteorol. Soc. Jpn.*, 82, 761–773, https://doi.org/10.2151/jmsj.2004.761, 2004.

Li, Y., Zhao, M. S., Motesharrei, S., Mu, Q. Z., Kalnay, E., and Li, S. C.: Local cooling and warming effects of forests based on satellite observations, *Nat. Commun.*, 6, 6603, https://doi.org/10.1038/ncomms7603, 2015.

https://doi.org/10.5194/egusphere-2026-1091
Preprint. Discussion started: 6 March 2026

Li, Z., Lau, W.K.-M., Ramanathan, V., Wu, G., Ding, Y., Manoj, M.G., Liu, J., Qian, Y., Li, J., Zhou, T., Fan, J., Rosenfeld, D., Ming, Y., Wang, Y., Huang, J., Wang, B., Xu, X., Lee, S.-S., Cribb, M., Zhang, F., Yang, X., Zhao, C., Takemura, T., Wang, K., Xia, X., Yin, Y., Zhang, H., Guo, J., Zhai, P.M., Sugimoto, N., Babu, S.S., and Brasseur, G.P.: Aerosol and monsoon climate interactions over Asia, *Rev. Geophys.*, 54, 866–929, https://doi.org/10.1002/2015RG000500, 2016.

Lu, H., Xie, M., Zhuang, B. L., Ma, D. Y., Liu, B. J., Zhan, Y. Z. H, Wang, T. J., Li, S., Li, M. M., and Zhu, K. G.: Impacts of atmospheric circulation patterns and cloud inhibition on aerosol radiative effect and boundary layer structure during winter air pollution in Sichuan Basin, China, *Atmos. Chem. Phys.*, 24, 8963–8982, https://doi.org/10.5194/acp-24-8963-2024, 2024.

Luo, Y., Zhang, R., Qian, W., Luo, Z., and Hu, X.: Intercomparison of deep convection over the Tibetan Plateau–Asian monsoon region and subtropical North America in boreal summer using CloudSat/CALIPSO data, *J. Clim.*, 24, 2164–2177, https://doi.org/10.1175/2010JCLI4032.1, 2011.

Ling, J., Liu, R., Wei, S., Chen, S. M., Ji, L. Y., Zhao, Y. C., and Zhang, H. S.: Cloud probability distribution of typical urban agglomerations in China based on Sentinel-2 satellite remote sensing, *Int. J. Appl. Earth. Obs.*, 135, 104254, https://doi.org/10.1016/j.jag.2024.104254, 2024.

LÜ, S. S., Zhou, Q., and Zhang, Y.: Comparison of cloud vertical structure retrieved from radiosonde and millimeter wave cloud radar, *Clim. Environ. Res*. (in Chinese), 26 (1), 18–30, https://doi.org/10.3878/j.issn.1006-9585.2020.19133, 2021.

Li, J. D., Geen, R., Mao, J. Y., Song, Y. J., Vallis, G. K., and Wu, G. X.: Mechanical and thermal forcings of Asian large-scale orography on spring cloud amount and atmospheric radiation budget over East Asia, *J. Clim.*, 36 (15), 5215–5232, https://doi.org/10.1175/JCLI-D-22-0797.1, 2023.

Li, H. Y., Liu, G. H., Han, C. T., Yang, Y., and Chen, R. S.: Quantifying the trends and variations in the frost-free period and the number of frost days across China under climate change using ERA5-Land reanalysis dataset, *Remote Sens.*, 14, 2400, https://doi.org/10.3390/rs14102400, 2022.

Li, J., Yu, R. C., and Zhou, T. J.: Seasonal variation of the diurnal cycle of rainfall in southern contiguous China, *J. Clim.*, 21 (22), 6036–6043, https://doi.org/10.1175/2008JCLI2188.1, 2008.

Liu, B., Guo, J., Gong, W., Shi, L., Zhang, Y., and Ma, Y.: Characteristics and performance of wind profiles as observed by the radar wind profiler network of China, *Atmos Meas. Tech.*, 13, 4589–4600, https://doi.org/10.5194/amt-13-4589-2020, 2020.

Liu, Y. J., and Ding, Y. H.: Analysis of basic features of the onset of the Asian summer monsoon, *J. Meteorol. Res.*, 21, 257–276, 2007.

https://doi.org/10.5194/egusphere-2026-1091
Preprint. Discussion started: 6 March 2026

Liu, Y. H.: Impacts of active satellite sensors' low-level cloud detection limitations on cloud radiative forcing in the Arctic, *Atmos. Chem. phys.*, 22 (12), 8151–8173, https://doi.org/10.5194/acp-22-8151-2022, 2022.

Lu., X., Mao, F. Y., Rosenfeld, D., Zhu, Y. N., Pan, Z. X., and Gong, W.: Satellite retrieval of cloud base height and geometric thickness of low-level cloud based on CALIPSO, *Atmos. Chem. Phys.*, 21, 11979–12003, https://doi.org/10.5194/acp-21-11979-2021, 2021.

Mace, G. G., Clothiaux, E. E., and Ackerman, T. P.: The composite characteristics of cirrus clouds: Bulk properties revealed by one year of continuous cloud radar data, *J. Clim.*, 14, 2185–2203, https://doi.org/10.1175/15200442(2001)014<2185:tccocc>2.0.co;2, 2001.

Mace, G. G., Benson, S., and Vernon, E.: Cirrus clouds and the large-scale atmospheric state: Relationships revealed by six years of ground-based data, *J. Clim.*, 19 (13), 3257–3278, https://doi.org/10.1175/JCLI3786.1, 2006.

Medeiros, B., Nuijens, L., Antoniazzi, C., and Stevens, B.: Low-latitude boundary layer clouds as seen by CALIPSO, *J. Clim.*, 115, D23207, https://doi.org/10.1029/2010JD014437, 2010.

Mellado, J. P., Stevens, B., and Schmidt, H.: Wind shear and buoyancy reversal at the top of stratocumulus, *J. Atmos. Sci.*, 71 (3), 1040–1057, https://doi.org/10.1175/JAS-D-13-0189.1, 2014.

Meng, D. L., Guo, J. P., Guo, X. R., Wang, Y. J., Li, N., Sun, Y. P., Zhang, Z., Tang, N., Li, H. R., Zhang, F., Tong, B., Xu, H., and Chen, T. M.: Elucidating the boundary layer turbulence dissipation rate using high-resolution measurements from a radar wind profiler network over the Tibetan Plateau, *Atmos. Chem. Phys.*, 24, 8703–8720, https://doi.org/10.5194/acp-24-8703-2024, 2024.

Mitra, A., Loveridge, J. R., and Di Girolamo, L.: Fusion of MISR stereo cloud heights and Terra-MODIS thermal infrared radiances to estimate two-layered cloud properties, *J. Geophys. Res.-Atmos.*, 128 (12), e2022JD038135, https://doi.org/10.1029/2022JD038135, 2023.

Muhlbauer, A., McCoy, I. L., and Wood, R.: Climatology of stratocumulus cloud morphologies: microphysical properties and radiative effects, *Atmos. Chem. Phys.*, 14 (13), 6695–6716, https://doi.org/10.5194/acp-14-6695-2014, 2014.

Mülmenstädt, J., Sourdeval, O., Henderson, D. S., L'Ecuyer, T. S., Unglaub, C., Jungandreas, L., Böhm, C., Russell, L. M., and Quaas, J.: Using CALIOP to estimate cloud-field base height and its uncertainty: the Cloud Base Altitude Spatial Extrapolator (CBASE) algorithm and dataset, *Earth Syst. Sci. Data*, 10, 2279–2293, https://doi.org/10.5194/essd-10-2279-2018, 2018.

Oreopoulos, L., Cho, N., and Lee, D.: New insights about cloud vertical structure from CloudSat and CALIPSO observations, *J. Geophys. Res.-Atmos.*, 122 (17), 9280–9300, https://doi.org/10.1002/2017JD026629, 2017.

https://doi.org/10.5194/egusphere-2026-1091
Preprint. Discussion started: 6 March 2026

Pan, Z., Gong, W., Mao, F., Li, J., Wang, W., Li, C. and Min, Q.: Macrophysical and optical properties of clouds over East Asia measured by CALIPSO, *J, Geophys. Res.-Atmos.*, 120 (22), 11–653. https://doi.org/10.1002/2015JD023735, 2015.

Pan, Z., Mao, F., Gong, W., Wang, W., and Yang, J.: Observation of clouds macrophysical characteristics in China by CALIPSO, Journal of Applied Remote Sensing, 10 (3), 036028. https://doi.org/10.1117/1.JRS.10.036028, 2016.

Pan, B. W., Liu, D. T., Du, Y. M., Zhao, D. L., Hu, K., Ding, S., Yu, C. J., Tian, P., Wu, Y. Z., Li, S. Y., and Kumar, K. R.: Intercomparisons on the vertical profiles of cloud microphysical properties from CloudSat retrievals over the North China Plain, *J. Geophys. Res.-Atmos.*, 128 (13), e2023JD039093, https://doi.org/10.1029/2023JD039093, 2023.

Ramanathan, V., Cess, R. D., Harrison, E. F., Minnis, P., Barkstrom, B. R., Ahmad, E., and Hartmann, D.: Cloud-radiative forcing and climate: Results from the earth radiation budget experiment, *Science*, 243, 57–63, https://doi.org/ 10.1126/science.243.4887.57, 1989.

Richardson, M. T., Roy, R. J., and Lebsock, M. D.: Satellites Suggest Rising Tropical High Cloud Altitude: 2002–2021, *Geophys. Res. Lett.*, 49 (10), e2022GL098160, https://doi.org/10.1029/2022GL098160, 2022.

Richardson, Y. P., Droegemeier, K. K., and Davies-Jones, R. P.: The influence of horizontal environmental variability on numerically simulated convective storms. Part I: Variations in vertical shear, *Mon. Weather Rev.*, 135, 3429–3455, https://doi.org/10.1175/MWR3463.1, 2007.

Sathiyamoorthy, V., Pal, P. K., and Joshi, P. C.: Influence of the upper-tropospheric wind shear upon cloud radiative forcing in the Asian monsoon region, *J. Clim.*, 17, 2725–2735, https://doi.org/10.1175/1520-0442(2004)017<2725:IOTUWS>2.0.CO;2, 2004.

Shepherd, J., Stallins, J. A., Jin, M. L., and Mote, T. L.: Urbanization: Impacts on clouds, precipitation, and lightning, *Urban Ecosyst. Ecol.*, 55, 1–28, https://doi.org/10.2134/agronmonogr55.c1, 2010.

Slingo, J. M.: The development and verification of a cloud prediction scheme for the ECMWF model, *Quart. J. Roy. Meteor. Soc.*, 113, 899–927, https://doi.org/10.1002/qj.49711347710, 2007.

Stephens, G. L.: Cloud feedbacks in the climate system: A critical review, *J. Clim.*, 18, 237–273, https://doi.org/10.1175/JCLI-3243.1, 2005.

Song, Y. L., Achberger, C., and Linderholm, H. W.: Rain-season trends in precipitation and their effect in different climate regions of China during 1961–2008, *Environ. Res. Lett.*, 6, 034025, https://doi.org/10.1088/1748-9326/6/3/034025, 2011.

https://doi.org/10.5194/egusphere-2026-1091
Preprint. Discussion started: 6 March 2026

Shi, Y., and Wang, G. L.: Changes in building climate zones over China based on high-resolution regional climate projections, *Environ. Res. Lett.*, 15, 114045, https://doi.org/10.1088/1748-9326/abbde8, 2020.

Spracklen, D. V., Arnold, S. R., and Taylor, C. M.: Observations of increased tropical rainfall preceded by air passage over forests, *Nature*, 489, 282–285, https://doi.org/10.1038/nature11390, 2012.

Stephens, G. L., Wild, M., Stackhouse, P. W., L'Ecuyer, T., Kato, S., and Henderson, D. S.: The global character of the flux of downward Longwave radiation., *J. Clim.*, 25 (7), 2329–2340, http://doi.org/10.1175/jcli-d-11-00262.1, 2012.

Syktus, J. I., and McAlpine, C. A.: More than carbon sequestration: Biophysical climate benefits of restored savanna woodlands, *Nature Sci. Rep.*, 6, 29194, https://doi.org/10.1038/srep29194, 2016.

Trivedi, P. K., van Hooff, J. T., Sierra Delgado, A., Laan, K. C. A., Smook, A. C., and van Daal, B. T.: Cloud-base heights over different land-use classes: Learnings of a distributed LogTag network in and around the Guatemalan Cloud Forest, TU Delft Student Rep., 2025, https://repository.tudelft.nl/record/uuid:4fb0dff2-6dfa-41b9-bca1-fc61af140f1c, 2025.

Thies, B., and Bendix, J.: Satellite based remote sensing of weather and climate: recent achievements and future perspectives, *Meteorol. Appl.*, 18, 262–295, https://doi.org/10.1002/met.288, 2011.

Voigt, A., Albern, N., Ceppi, P., Grise, K., Li, Y., and Medeiros, B.: Clouds, radiation, and atmospheric circulation in the present-day climate and under climate change, *Wires. Clim. Change*, 12, e694, https://doi.org/10.1002/wcc.694, 2021.

Wang, Z., and Sassen, K.: Cloud type and macrophysical property retrieval using multiple remote sensors, *J. Appl. Meteor.*, 40 (10), 1665–1682, https://doi.org/10.1175/1520-0450(2001)040<1665:CTAMPR>2.0.CO;2, 2001.

Wang, Y., and Wang, C. H.: Features of clouds and convection during the pre- and post-onset periods of the Asian summer monsoon, *Theor. Appl. Climatol.*, 123, 551–564, https://doi.org/10.1007/s00704-015-1372-7, 2016.

Wang, Z., Wang, Z. H., and Cao, X. Z.: Consistency analysis for cloud vertical structure derived from millimeter cloud radar and radiosonde profiles, *Acta Meteorol. Sin.*, 74 (5), 815–826, https://doi.org/10.11676/qxxb2016.057, 2016.

Wang, D., Guo, J. P., Xu, H., Li, J., Lv, Y. M., Solanki, R., Guo, X. R., Han, Y., Chen, T. M., Ding, M. H., Chen, A. J., Bian, L. G., and Rinke, A.: Vertical structures of temperature inversions and clouds derived from high-resolution radiosonde measurements at Ny-Ålesund, Svalbard, *Atmos. Res.*, 254, 105530, https://doi.org/10.1016/j.atmosres.2021.105530, 2021.

https://doi.org/10.5194/egusphere-2026-1091
Preprint. Discussion started: 6 March 2026

Weisman, M. L., and Rotunno, R.: The use of vertical wind shear versus helicity in interpreting supercell dynamics, *J. Atmos. Sci.*, 57 (9), 1452–1472, https://doi.org/10.1175/1520-0469(2000)057<1452:TUOVWS>2.0.CO;2, 2000.

Weare, B. C.: Insights into the importance of cloud vertical structure in climate, *Geophys. Res. Lett.*, 27(6), 907–910, https://doi.org/10.1029/1999GL011214, 2000.

Williams, K. D., Ringer, M. A., Senior, C. A., Webb, M. J., McAvaney, B. J., Andronova, N., Bony, S., Dufresne, J. L., Emori, S., and Gudgel, R.: Evaluation of a component of the cloud response to climate change in an intercomparison of climate models, *Clim. Dyn.*, 26, 145–165, https://doi.org/10.1007/s00382-005-0067-7, 2006.

Wielicki, B. A., Cess, R. D., King, M. D., Randall, D. A., and Harrison, E. F.: Mission to planet Earth: Role of clouds and radiation in climate, *Bull. Amer. Meteor. Soc.*, 76 (11), 2125–2154, https://doi.org/10.1175/1520-0477(1995)076<2125:MTPERO>2.0.CO;2, 1995.

Wild, M.: New Directions: A facelift for the picture of the global energy balance, *Atmos. Environ.*, 55, 366–367, https://doi.org/10.1016/j.atmosenv.2012.03.022, 2012.

Williams, A. P., Schwartz, R. E., Iacobellis, S., Seager, R., Cook, B. I., Still, C.J., Husak, G., and Michaelsen, J.: Urbanization causes increased cloud base height and decreased fog in coastal Southern California, *Geophys. Res. Lett.*, 42, 1527–1536, https://doi.org/10.1002/2015GL063266, 2015.

Wood, R., and Bretherton, C. S.: On the relationship between stratiform low cloud cover and lower-tropospheric stability, *J. Clim.*, 19, 6425–6432, https://doi.org/10.1175/JCLI3988.1, 2006.

Xu, R. Li, Y., Teuling, A. J., Spracklen, D. V., Garcia-Carreras, L., Meier, R., Chen, L., Zheng, Y. T., Lin, H. Q., and Fu, B. J.: Contrasting impacts of forests on cloud cover based on satellite observations, *Nat. Commun.*, 13, 670, https://doi.org/10.1038/s41467-022-28161-7, 2022.

Xu, H., J. Guo, J. Li, L. Liu, T. Chen, X. Guo, Y. Lv, D. Wang, Y. Han, Q. Chen, Y. Zhang: Significant Role of Radiosonde-measured Cloud-base Height in Estimating Cloud Radiative Forcing, *Adv. Atmos. Sci.,* 38 (9), 1552–1565, https://doi.org/10.1007/s00376-021-0431-5, 2021.

Xu, H., Guo, J., Tong, B., Zhang, J., Chen, T., Guo, X., Zhang, J., and Chen, W.: Characterizing the near-global cloud vertical structures over land using high-resolution radiosonde measurements, *Atmos. Chem. Phys.*, 23, 15011–15038, https://doi.org/10.5194/acp-23-15011-2023, 2023.

Xu, H., Guo, J., Chen, T., Wang, Y., Deng, J., and Tong, B.: Do aerosols induce the differences in low cloud frequency between eastern China and eastern United States? *Atmos. Res.*, 318, 107994, https://doi.org/10.1016/j.atmosres.2025.107994, 2025.

https://doi.org/10.5194/egusphere-2026-1091
Preprint. Discussion started: 6 March 2026

Yang, Y., Chen, R., Han, C., and Liu, Z.: Evaluation of 18 models for calculating potential evapotranspiration in different climatic zones of China, *Agric. Water Manag.*, 244, 106545, https://doi.org/10.1016/j.agwat.2020.106545, 2021.

Yang, J., Liu, E. H., Liu, Y. B., Lin, Y. J., Yin, Y., and Jing, X. Q.: Impact of vertical wind shear on summer orographic clouds over Tian Shan Mountains: A case study based on radar observation and numerical simulation, *Remote Sens.*, 14 (7), 1583, https://doi.org/10.3390/rs14071583, 2022.

Yu, R., Yu, Y., and Zhang, M.: Comparing cloud radiative properties between the eastern China and the Indian monsoon region, *Adv. Atmos. Sci.*, 18, 1090–1101, https://doi.org/10.1007/s00376-001-0025-1, 2001.

Zhao, W., Marchand, R., and Fu, Q.: The diurnal cycle of clouds and precipitation at the ARM SGP site: Cloud radar observations and simulations from the multiscale modeling framework, *J. Geophys. Res.-Atmos.*, 122 (14), 7519–7536, https://doi.org/10.1002/2016JD026353, 2017.

Zhao, C. F., Chen, Y. Y., Li, J. M., Letu, H., Su, Y. F., Chen, T. M., and Wu, X. L.: Fifteen-year statistical analysis of cloud characteristics over China using Terra and Aqua Moderate Resolution Imaging Spectroradiometer observations, *Int. J. Climatol.*, 39 (5), 2612–2629, https://doi.org/10.1002/joc.5975, 2019.

Zhou, Q., Zhang, Y., Li, B., Li, L. X., Feng, J. M., Jia, S. Z., Lv, S. S., Tao, F., and Guo, J.: Cloud-base and cloud-top heights determined from a ground-based cloud radar in Beijing, China, *Atmos. Enviorn.*, 201, 381–390, https://doi.org/10.1016/j.atmosenv.2019.01.012, 2019.

Zhang, C., Zhao, D. F., Gao, Y. H., Song, Z., Zhao, B., and Wang, G. Y.: Increasing summertime low-level cloud cover associated with increasing vegetation in China from 2003 to 2022, *Environ. Res. Lett.*, 19, 124061, https://doi.org/10.1088/1748-9326/ad8cee, 2024.

Zhang, R., Sumi, A., and Kimoto, M.: Impact of El Niño on the East Asian monsoon: A diagnostic study of the '86/87 and '91/92 events, *J. Meteor. Soc. Japan*, 74 (1), 49–62, https://doi.org/10.2151/jmsj1965.75.1_125, 1996.

Zhou, X. X., Xie, B., Zhang, H., He, J. Y., and Chen, Q.: Decomposition of fast and slow cloud responses to quadrupled CO_2 forcing in BCC-AGCM2.0 over East Asia, *Adv. Atmos. Sci.*, 39 (12), 2188–2202, https://doi.org/10.1007/s00376-022-1441-7, 2022.

Zhang, Y., and Klein, S. A.: Factors controlling the vertical extent of fair-weather shallow cumulus clouds over land: Investigation of diurnal-cycle observations collected at the ARM Southern Great Plains site, *J. Atmos. Sci.*, 70, 1297–1315, https://doi.org/10.1175/JAS-D-12-0131.1, 2013.

Zhang, Y., Zhang, L. J., Guo, J. P., Feng, J. M., Cao, L. J., Wang, Y., Zhou, Q., Li, L. X., Li, B., Xu, H., Liu, L., An, N., and Liu. H.: Climatology of cloud-base height from long-term radiosonde

https://doi.org/10.5194/egusphere-2026-1091
Preprint. Discussion started: 6 March 2026

measurements in China, *Adv. Atmos. Sci.*, 35, 158−168, https://doi.org/10.1007/s00376-017-7096-0, 2018.

Zhang, Y., Zhou, Q., Lv, S. S., Jia, S. Z., Tao, F., Chen, D. D., and Guo, J. P.: Elucidating cloud vertical structures based on three-year Ka-band cloud radar observations from Beijing, China, *Atmos. Res.*, 222, 88–99, https://doi.org/10.1016/j.atmosres.2019.02.007, 2019.

https://doi.org/10.5194/egusphere-2026-1091
Preprint. Discussion started: 6 March 2026

Figures

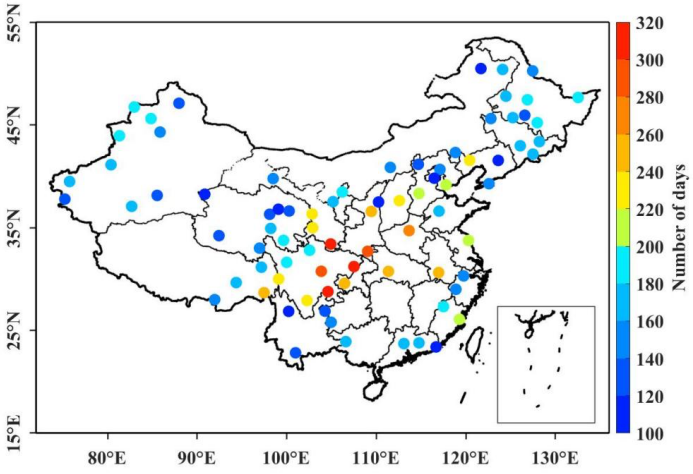

Figure 1. Geographical distribution of millimeter-wave cloud radar (MMCR) stations across mainland China in 2024. A total of 120 MMCR stations were in nationwide operation during this period. For rigorous data quality control, stations with fewer than 100 valid annual observation days were excluded from the subsequent analysis. Consequently, 80 stations that met this quality criterion are displayed in the map, where the color of each station marker denotes the total number of days with valid observational records at the corresponding site.

https://doi.org/10.5194/egusphere-2026-1091
Preprint. Discussion started: 6 March 2026

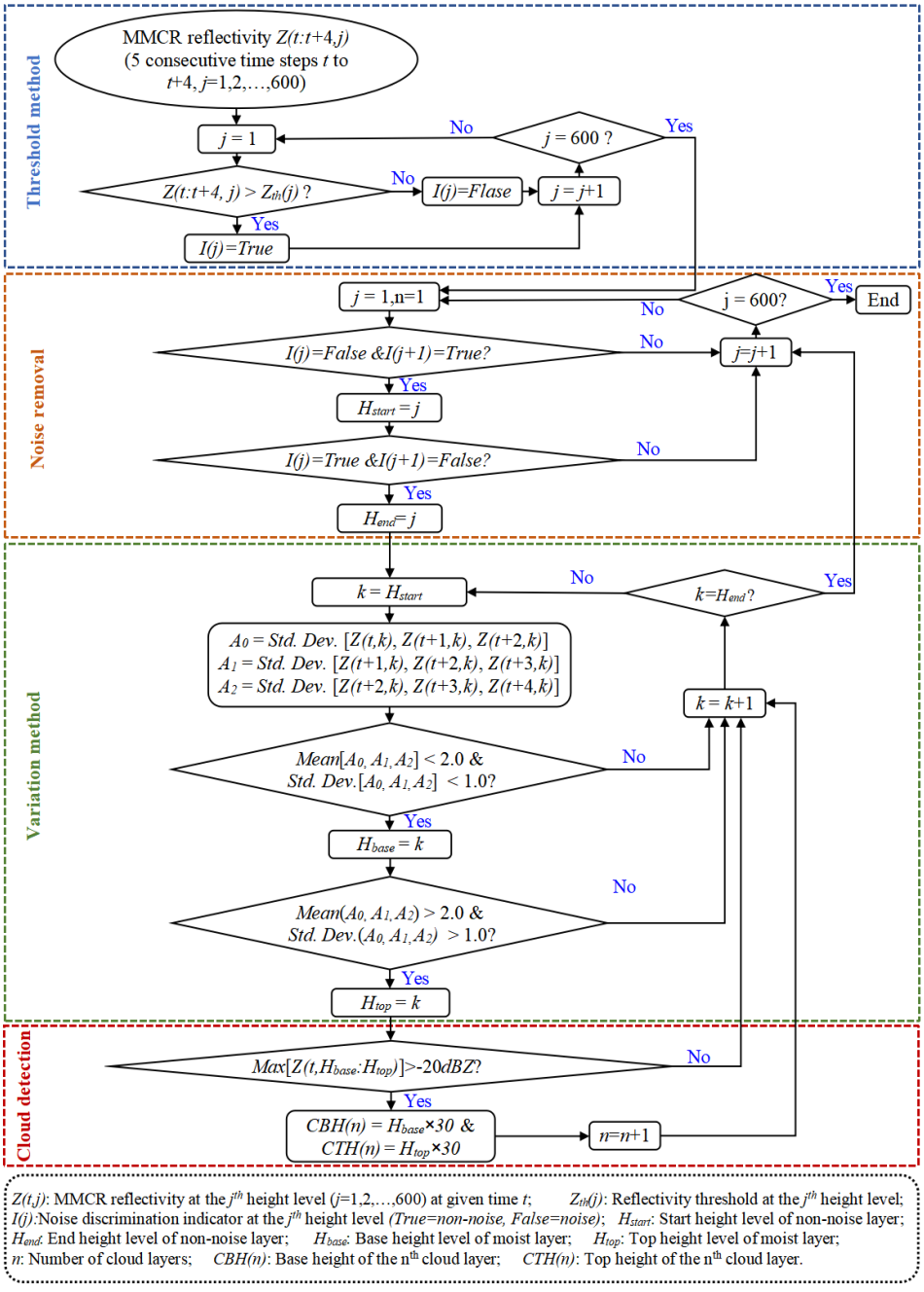

Figure 2. Flowchart for identifying the cloud vertical structure (CVS) from high-temporal-resolution MMCR measurements. This flowchart comprises four sequential key steps in the CVS retrieval process: first, the threshold method involves comparing the MMCR reflectivity $Z(t: t+4, j)$ against the height-

https://doi.org/10.5194/egusphere-2026-1091
Preprint. Discussion started: 6 March 2026

dependent threshold $Z_{th}(j)$ to generate the noise discrimination indicator $I(j)$, which distinguishes non-noise and noise layers; subsequently, the noise removal step identifies the start (H_{start}) and end (H_{end}) height levels of non-noise layers based on the indicator $I(j)$; then, the variation method determines the base (H_{base}) and top (H_{top}) height levels of moist layers by calculating the statistical variation (including standard deviation and mean) of reflectivity within the identified non-noise layers; finally, the cloud detection step retrieves the base height ($CBH(n)$) and top height ($CTH(n)$) of each cloud layer by verifying the reflectivity magnitude of the moist layers, thereby yielding the final cloud vertical structure.

https://doi.org/10.5194/egusphere-2026-1091
Preprint. Discussion started: 6 March 2026

1127

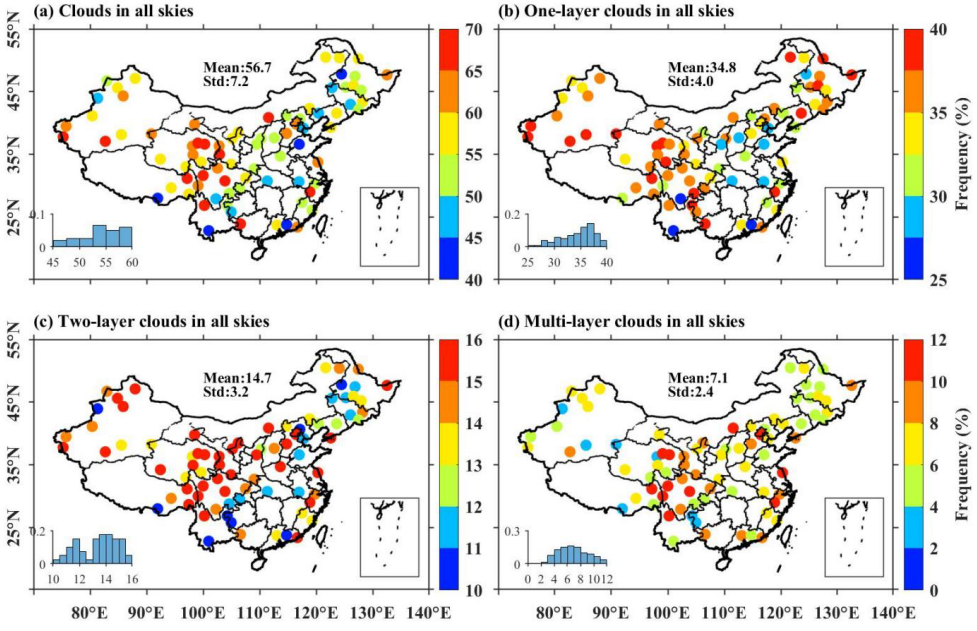

1128

1129 **Figure 3.** Spatial distribution of annual mean cloud occurrence frequency for different cloud layering
1130 classifications: (a) all clouds, (b) single-layer clouds, (c) two-layer clouds, and (d) multi-layer clouds
1131 (three-, four-, and five-layer clouds) under all-sky conditions in 2024. The data are derived from the 80
1132 MMCR stations presented in Figure 1. Notably, the color bars are scaled independently across panels to
1133 improve visual clarity. In addition, each panel show the histograms depicting the probability distributions
1134 of cloud occurrence frequencies, with the corresponding mean values and standard deviations also
1135 presented for each distribution.

1136

https://doi.org/10.5194/egusphere-2026-1091
Preprint. Discussion started: 6 March 2026

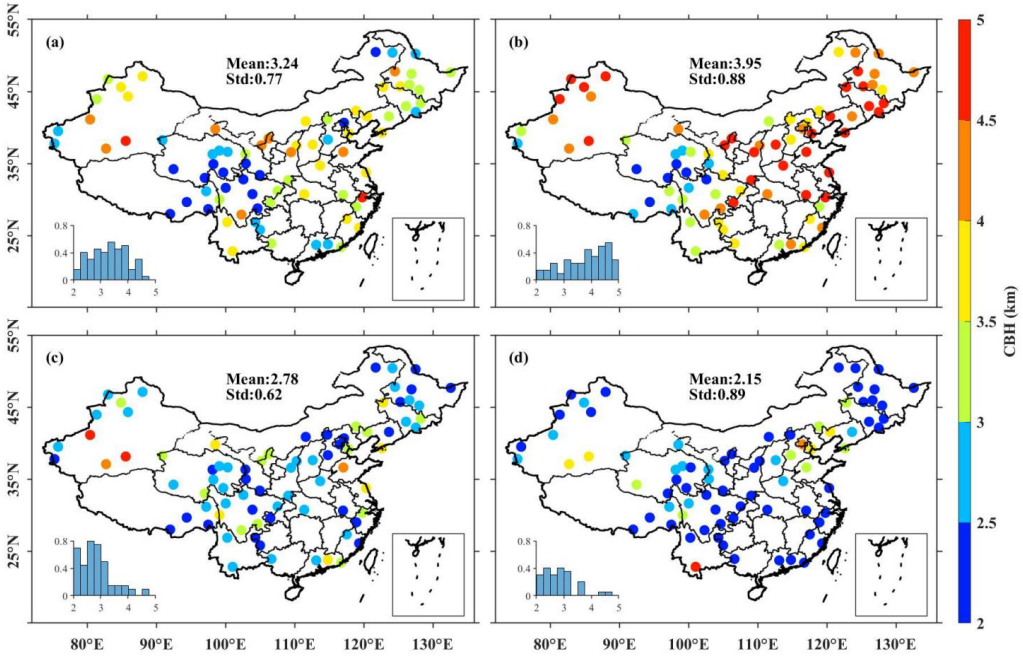

Figure 4. Seasonal geographic distribution of cloud base height (CBH) over China in 2024, derived from the 80 MMCR stations of the same network referenced in Figure 1. The four panels correspond to (a) spring (March–April–May), (b) summer (June–July–August), (c) autumn (September–October–November), and (d) winter (December–January–February). Note that each panel presents a histogram illustrating the probability distribution of cloud occurrence frequency, with the corresponding mean value and standard deviation provided for each distribution.

https://doi.org/10.5194/egusphere-2026-1091
Preprint. Discussion started: 6 March 2026

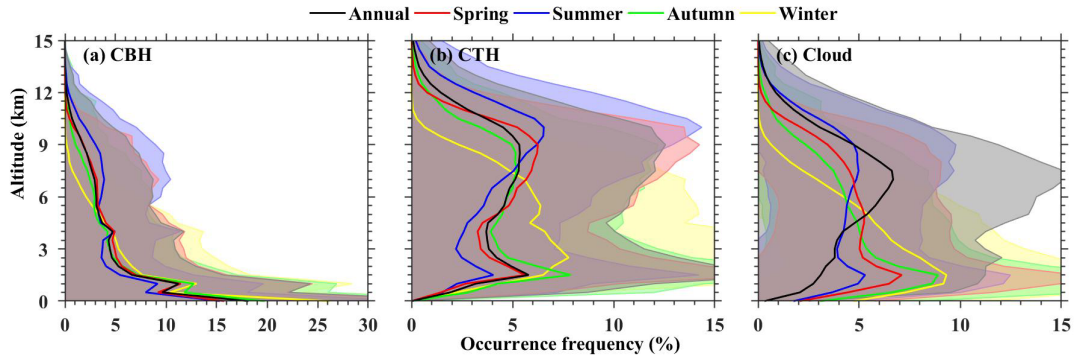

Figure 5. Vertical distributions of annual and seasonal mean occurrence frequencies of (a) CBH and (b) cloud top height (CTH), and (c) overall cloud occurrence across China in 2024. The annual mean is plotted in black, while seasonal means for spring, summer, autumn, and winter are shown in red, blue, green, and yellow, respectively. Data samples are binned at a vertical resolution of 200 m. At each altitude, cloud occurrence frequency is defined as the ratio of cloudy samples at that altitude to the total number of cloudy samples across all altitudes. Solid lines denote mean values, and shaded areas represent the corresponding standard deviations.

https://doi.org/10.5194/egusphere-2026-1091
Preprint. Discussion started: 6 March 2026

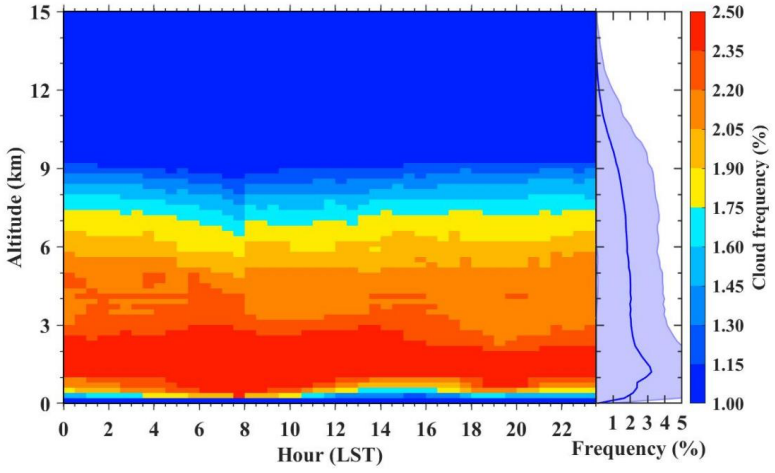

Figure 6. Annual mean diurnal cycle of height-resolved cloud occurrence frequency and corresponding vertical profiles derived from measurements at all 80 MMCR stations (Figure 1) across China in 2024. Data samples are binned at a vertical resolution of 200 m and a temporal resolution of 30 minutes. Cloud occurrence frequency at a given altitude is defined as the ratio of cloudy samples at that altitude to the total number of cloudy samples across all altitudes. Also presented are the corresponding vertical probability distributions of clouds.

https://doi.org/10.5194/egusphere-2026-1091
Preprint. Discussion started: 6 March 2026

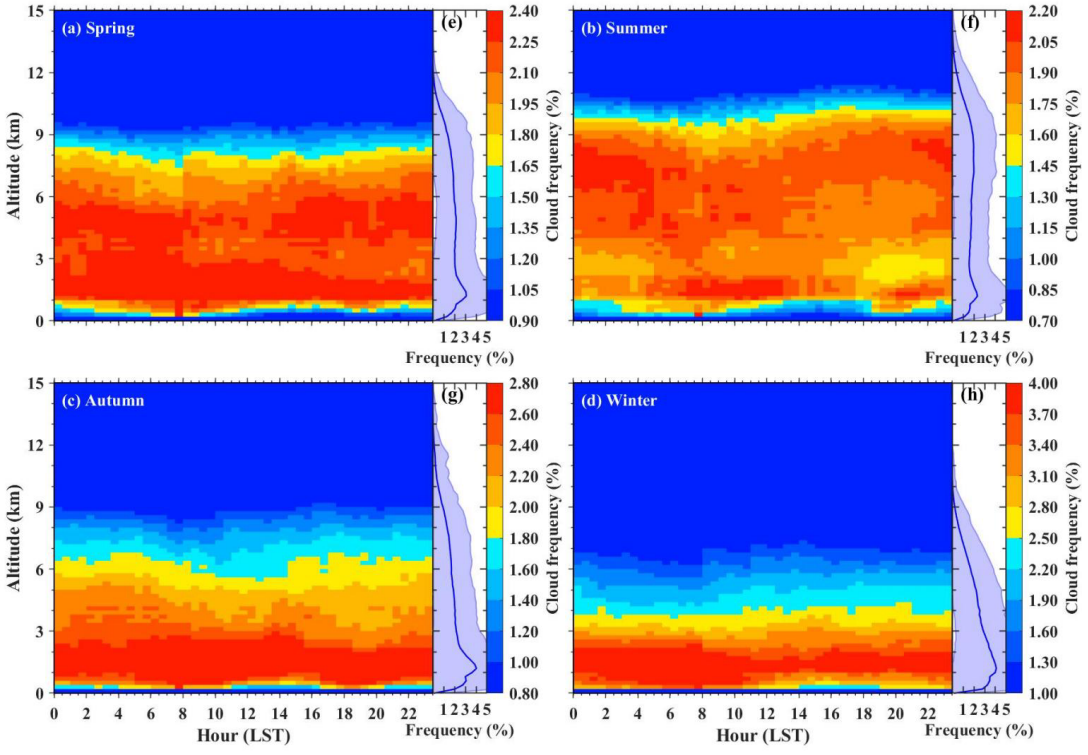

Figure 7. Similar to Figure 6, but for the seasonal mean diurnal cycle of height-resolved cloud occurrence frequency and corresponding vertical profiles over China in (a) spring, (b) summer, (c) autumn, and (d) winter.

https://doi.org/10.5194/egusphere-2026-1091
Preprint. Discussion started: 6 March 2026

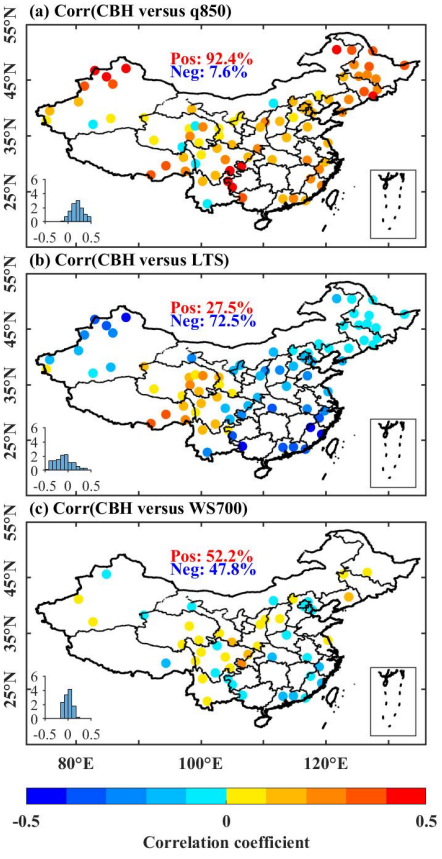

Figure 8. Spatial correlations of CBH, CTH, and cloud thickness (CT) with lower-tropospheric stability (LTS), specific humidity at 850 hPa (q_{850}), and 700 hPa vertical wind shear (WS_{700}) across China (2024). All atmospheric variables were spatially and temporally matched with the MMCR CBH observational data to ensure the reliability of the correlation analysis. In each panel, the probability distribution of the correlation coefficient is illustrated by a histogram, and the abbreviations "Pos" and "Neg" denote the percentages of statistically significant positive and negative correlation coefficients across the entire study domain, respectively.

https://doi.org/10.5194/egusphere-2026-1091
Preprint. Discussion started: 6 March 2026

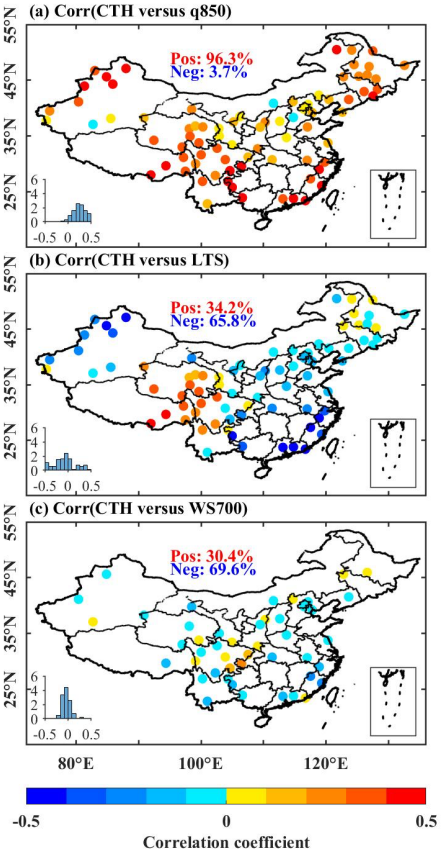

Figure 9. Similar as Figure 8, but for the CTH.

https://doi.org/10.5194/egusphere-2026-1091
Preprint. Discussion started: 6 March 2026

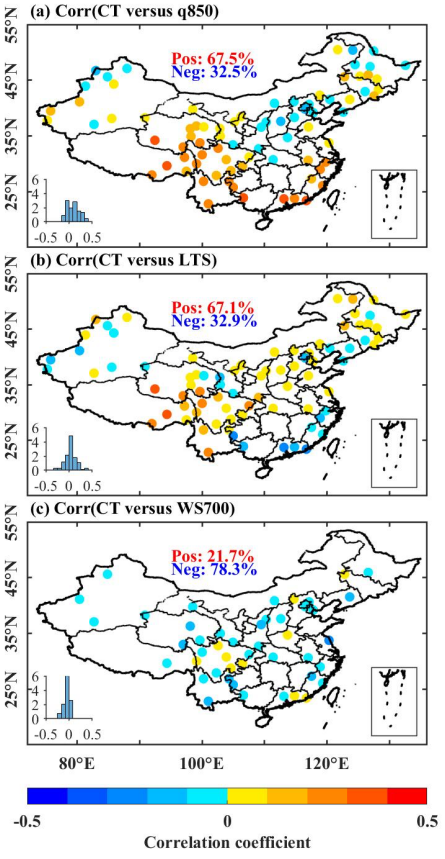

Figure 10. Similar as Figure 8, but for CT.

https://doi.org/10.5194/egusphere-2026-1091
Preprint. Discussion started: 6 March 2026

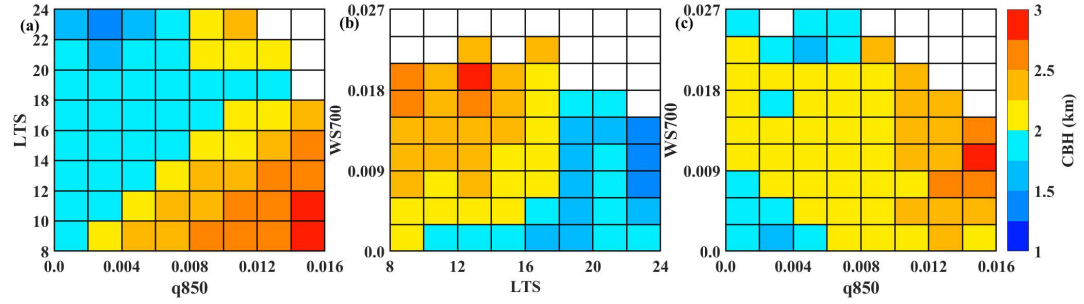

Figure 11. Bivariate regulation of CBH by thermodynamic and dynamical factors across China in 2024, based on observations from 80 MMCR stations. Each panel illustrates the response of CBH to the combined modulating effects of a specific pair of key atmospheric factors: (a) LTS and q_{850}, (b) WS700 and LTS, and (c) WS_{700} and q_{850}. All ERA5 reanalysis variables were spatially and temporally matched with MMCR data to ensure the validity and reliability of this bivariate joint dependence analysis.

https://doi.org/10.5194/egusphere-2026-1091
Preprint. Discussion started: 6 March 2026

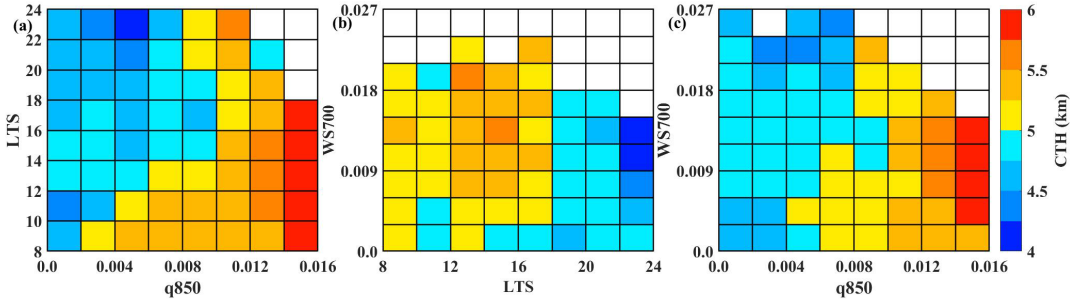

Figure 12. Similar as Figure 11, but for CTH.

https://doi.org/10.5194/egusphere-2026-1091
Preprint. Discussion started: 6 March 2026

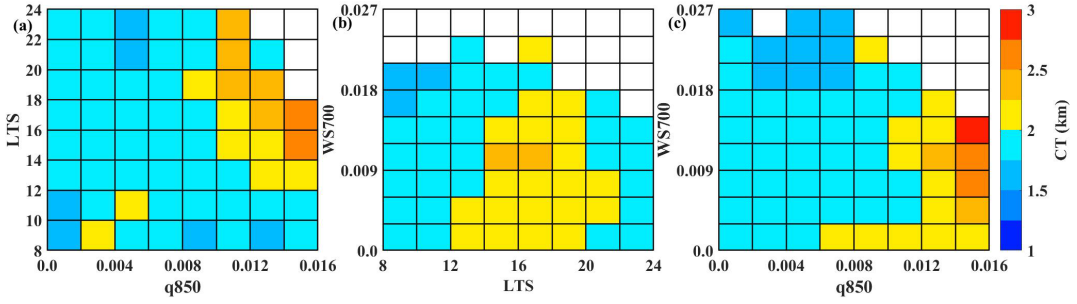

Figure 13. Similar as Figure 11, but for CT.

https://doi.org/10.5194/egusphere-2026-1091
Preprint. Discussion started: 6 March 2026

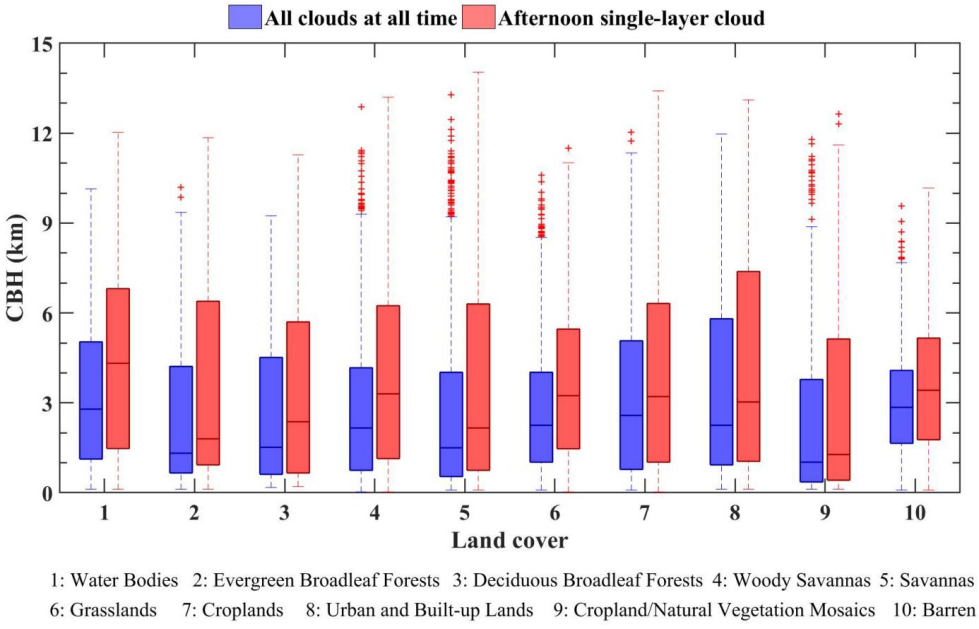

Figure 14. Land-surface influence on CBH across China in 2024, based on 80 MMCR stations. Blue bars indicate all-sky conditions, and red bars represent afternoon single-layer clouds. Land cover types are derived from the MODIS Land Cover Type Yearly Climate Modeling Grid product (MCD12C1; https://lsdsweb.modaps.eosdis.nasa.gov/missions-and-measurements/products/MCD12C1).

https://doi.org/10.5194/egusphere-2026-1091
Preprint. Discussion started: 6 March 2026

1207

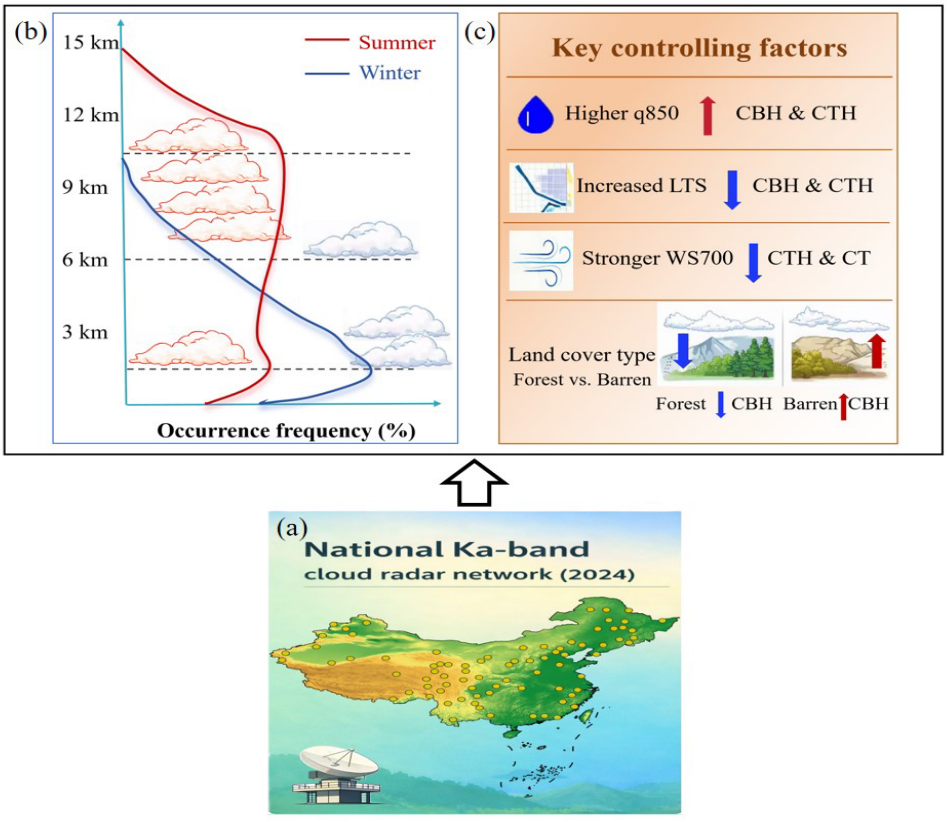

1208

1209 **Figure 15**. Schematic diagram illustrating the characteristics and controlling factors of cloud vertical
1210 structure (CVS) over China, as observed by the national Ka-band cloud radar network. (a) Spatial
1211 distribution of the national Ka-band cloud radar network established in 2024. (b) Vertical profiles of cloud
1212 occurrence frequency for summer (red) and winter (blue), highlighting seasonal differences in cloud
1213 vertical distribution. (c) Key thermodynamic, dynamical, and land-surface factors controlling CVS, with
1214 upward and downward arrows indicating the corresponding increases and decreases in CBH, CTH, and
1215 CT.

1216

1217